JGR Solid Earth

Key Points:

- We have 3D printed over two hundred samples containing voids of various sizes, shapes, and orientations
- Samples were uniaxially compressed and their measured effective elastic properties were compared with predictions from Effective Medium Theory (EMT)
- Measured effective elastic moduli can fit EMT predictions with an error of less than 5%

Correspondence to:

A. Stanton-Yonge,
ashley.sesnic.18@ucl.ac.uk

Author Contributions:

Conceptualization: Filip P. Adamus, Thomas M. Mitchell, David Healy
Data curation: Filip P. Adamus, Ashley Stanton-Yonge
Formal analysis: Filip P. Adamus, Ashley Stanton-Yonge
Funding acquisition: Thomas M. Mitchell, David Healy, Philip G. Meredith
Investigation: Filip P. Adamus, Ashley Stanton-Yonge, Thomas M. Mitchell
Methodology: Filip P. Adamus, Ashley Stanton-Yonge, Thomas M. Mitchell, David Healy
Project administration: Thomas M. Mitchell, David Healy, Philip G. Meredith
Resources: Thomas M. Mitchell
Software: Filip P. Adamus, Ashley Stanton-Yonge

Uniaxial Compression of 3D Printed Samples With Voids: Laboratory Measurements Compared With Predictions From Effective Medium Theory

Filip P. Adamus[1] [ID], **Ashley Stanton-Yonge**[1,2] [ID], **Thomas M. Mitchell**[1] [ID], **David Healy**[3], and **Philip G. Meredith**[1] [ID]

[1]Department of Earth Sciences, University College London, London, UK, [2]Dipartimento di Geoscienze, Università degli Studi di Padova, Padua, Italy, [3]Geosolutions Leeds, School of Earth & Environment, University of Leeds, Leeds, UK

Abstract 3D printing technology offers the possibility of producing synthetic samples with accurately defined microstructures. As indicated by effective medium theory (EMT), the shapes, orientations, and sizes of voids significantly affect the overall elastic response of a solid body. By performing uniaxial compression tests on 20 types of 3D-printed samples containing voids of different geometries, we examine whether the measured effective elasticities are accurately predicted by EMT. To manufacture the sample, we selected printers that use different technologies; fused deposition modelling (FDM), and stereolithography (SLA). We show how printer settings (FDM case) or sample cure time (SLA case) affect the measured properties. We also examine the reproducibility of elasticity tests on identically designed samples. To obtain the range of theoretical predictions, we assume either uniform strain or uniform stress. Our study of over two hundred samples shows that measured effective elastic moduli can fit EMT predictions with an error of less than 5% using both FDM and SLA methods if certain printing specifications and sample design considerations are taken into account. Notably, we find that the pore volume fraction of the designed samples should be above ≈1% to induce a measurable softening effect, but below ≈5% to produce accurate EMT estimations that fit the measured elastic properties of the samples. Our results highlight both the strengths of EMT for predicting the effective properties of solids with low pore fraction volume microstructural configurations, and the limitations for high porosity microstructures, particularly, those with interactive pores geometries.

Plain Language Summary The mechanical strength of solid materials can be greatly influenced by the presence of cavities or voids within them. These voids tend to weaken the material, a phenomenon that can be estimated using effective medium approximations—mathematical models that predict the overall properties of materials with inhomogeneous internal structures. In this study, we compared theoretical predictions for the elastic properties of solids containing voids of different shapes and sizes with actual measurements taken from 3D-printed samples designed to replicate the same pore structures used in our calculations. We found that the predictions closely matched the measured elastic modulus, with an error of less than 5%. However, the accuracy of the results was affected by the choice of 3D printing technology and printing settings. Overall, our study confirms the use of effective medium approximations and provides a foundation for future research involving 3D printing to replicate rocks with complex internal pore structures.

1. Introduction

The elasticity of a material containing voids (empty pores) or inclusions (fluid-filled or solid pores) can be approximated using effective medium theory (EMT). The theory allows one to homogenize a medium and view its response on a larger scale. In turn, understanding how the microstructure (pores shape, orientation, and size) influences the overall response is beneficial in many disciplines, such as materials science, biomechanics, rock mechanics, seismology, oil and gas exploration, among others.

Probably the first steps in treating a material as effectively elastic were done by Voigt (1889), Reuss (1929), and Bruggeman (1937). Their works were followed and greatly developed by Hill (1952), Eshelby (1957), Hashin (1959), and Bristow (1960); researchers inspired by problems in metallurgy. Subsequently, their averaging approach was expanded by Walsh (1965), Budiansky (1965), Hill (1965), O'Connell and Budiansky (1974), Kachanov (1980), Oda et al. (1984), Zimmerman (1986), and Sayers and Kachanov (1991) who described how the specific geometry of ellipsoidal pores and cracks affect the stiffness (compliance) of a solid; a

Supervision: Thomas M. Mitchell, David Healy, Philip G. Meredith
Validation: Filip P. Adamus, Ashley Stanton-Yonge
Visualization: Filip P. Adamus, Ashley Stanton-Yonge
Writing – original draft: Filip P. Adamus, Ashley Stanton-Yonge
Writing – review & editing: Thomas M. Mitchell, David Healy, Philip G. Meredith

rock in particular. Independent efforts were made in the field of seismology by Postma (1955), Backus (1962), Schoenberg and Douma (1988), and Schoenberg and Helbig (1997), who focused on layered inhomogeneities or long and thin cracks instead of ellipsoidal shapes. Nevertheless, their approaches give approximately equal predictions when the layered features are viewed as a series of aligned penny-shaped cracks (Schoenberg & Douma, 1988). All effective elasticity approximations utilized by the aforementioned authors—and numerous researchers not mentioned herein—share the same concept, that the elasticity of the constituents (i.e., solid matrix and inhomogeneities) can be averaged to predict the overall medium's stiffness under given boundary conditions. Because there is no single recipe on how to do it, authors often use the notion of "effective medium theory" to refer to this general concept of averaging. The EMT goes beyond elasticity, with its origins in electromagnetic properties of materials; it makes an essential part of a multidisciplinary field called micromechanics (Kachanov & Sevostianov, 2018).

The EMT prediction for even the simple scenario of a single void embedded in a homogeneous matrix is not straightforward. The approximation is unequivocal only if (a) the background is isotropic or transversely isotropic, (b) the void is ellipsoidal, and (c) the void is very small. In the case that one of the first two conditions is not satisfied, an analytical solution cannot be obtained (Kachanov & Sevostianov, 2018). In the case that the void is relatively large, then the prediction will vary depending on the assumption chosen, due to the boundary effects (Hill, 1952). Then, the so-called apparent, and not effective, elasticity parameters are considered (Huet, 1990). One possibility is to assume uniform strain throughout the sample. Another is to assume uniform stress. Either assumption leads to an approximately identical result if the inhomogeneity is small, but are discrepant for larger sizes. This discrepancy also arises if there are more than one void that interact with each other, thus disturbing the stress and strain fields. If the distribution of voids is sparse, then the so-called non-interactive approximations are proposed (Kachanov, 1992). If voids are close together or even overlapping slightly, the interaction effect needs to be taken into consideration (Hill, 1965).

Early studies on ceramics with spherical pores have confirmed empirically the usefulness of EMT (Walsh, 1965). However, empirical validation becomes more difficult in the case of strongly oblate or prolate spheroids, shapes that may be good approximations for cracks present in for example, rocks. Because geomaterials usually have complex microstructures, the empirical validation of EMT using rocks is limited. For instance, we can verify that cracks of known orientation reduce the magnitude of specific parameters in the elasticity tensor (Brantut & Petit, 2022; Markov et al., 2006; Sayers & Kachanov, 1995), and therefore weaken the rocks, as predicted by the theory. However, the magnitude of the effect remains difficult to evaluate due to uncertainties in crack geometries, crack concentration, and crack interactions.

Attempts to examine EMT on synthetic materials, where the microstructure can be much better constrained, include placing polymeric inhomogeneities inside a previously prepared sandy matrix, with the polymeric materials being subsequently removed by chemical or thermal processes, leaving voids behind (Santos et al., 2017), and the use of rubber pieces placed in epoxy glass (Henriques et al., 2018). Alternatively, laser etching can be used to create cracks in glass (Stewart et al., 2013), or the geometry of cracked glass can be determined using Scanning Electron Microscopy (Mallet et al., 2013). Efforts of using additive manufacturing techniques for EMT validation purposes have employed either acoustic measurements of 3D printed samples containing ellipsoidal cracks (Dugarov et al., 2022; Huang et al., 2016; Ndao et al., 2017) or uniaxial tension/compression experiments of synthetic samples containing isotropic arrays of spherical/elliptical voids (Peloquin et al., 2023; Zerhouni, 2019). While these works have revealed crucial insights on the predictive capabilities of EMT, they have been restricted to small inhomogeneities only. This is because pores of a much smaller size than the wavelength are required for acoustic measurements in order to satisfy the quasi-static assumption of EMT. This way, a full elasticity tensor can be obtained at the expense of inaccuracy in the manufacture of small pores. Apart from the inaccuracy in microstructure design, small pores do not soften the material significantly and limit the possibility of validating the non-interaction approximation. In other words, small pores must be densely packed in order to obtain a measurable weakening effect on stiffnesses. In turn, one cannot clearly distinguish the impact of interactions from the effect of pore concentration itself. Also, the small size of pores impedes fluid injection to measure the poroelastic response of such samples. All the aforementioned problems can be overcome if larger inhomogeneities are considered. A downside of such a solution, though, is that the acoustic measurements are heavily degraded due to the static assumption violation. Also, the theoretical prediction is not unequivocal due to the impact of the choice of boundary conditions.

In this paper, we used fused deposition modelling (FDM) and stereolithography (SLA), two standard 3D printing technologies, to produce 20 different types of samples that contain relatively large voids with different geometries, including spherical, oblate, and prolate ellipsoidal pores with a variety of sizes, aspect ratios, and orientations. Samples were then uniaxially compressed to obtain the elastic components of the stiffness matrix (Young's modulus and Poisson's ratio), which were compared with theoretical predictions to test EMT empirically. Our research fills the gap in experimental studies on effective elasticity for several reasons. First, void geometries were designed to be large enough to enhance the softening effect and overcome measurement errors, instead of using dense microcracks only. Also, we propose various pore interaction configurations that have not been previously examined experimentally. In addition, the sizes of voids might facilitate future tests involving fluid injection into pores for direct measurement of poroelastic parameters. Finally, we report results from over two hundred samples, which enhances the robustness of our experimental validation and minimizes susceptibility to random errors. In addition, we discuss three main issues regarding uniaxial compression tests of 3D-printed samples with voids. First, we attempt to understand how the differences between 3D printing technologies and their specifications may affect the effective Young's modulus measurements. Second, we present the impact of Young's modulus computation methodology. Third, and most importantly, we focus on whether EMT accurately predicts Young's modulus given the issues mentioned above.

2. Materials and Methods

2.1. 3D Printing Technologies

3D printing has revolutionized the manufacturing industry, and numerous different printing technologies have emerged during the past decades. These technologies range in price, accessibility, post-printing processing requirements, printing resolution, surface finishing quality, and environmental impact. Two standard 3D printing technologies were used in this study: stereolithography (SLA) and Fused Deposition Modelling (FDM).

SLA is a type of additive manufacturing process that employs a laser source to solidify liquid-state, light-reactive resin into solid polymers through a process called photopolymerization. A Computer-Aided Design (CAD) model is imported into the 3D printer which then constructs the object layer by layer with 0.1 mm resolution. The resulting products usually require post-printing treatment. They are first immersed in isopropyl alcohol (IPA) to remove any residual, uncured resin. Subsequently, an additional curing step under heat may be needed to finalize the polymerization reaction, which brings the material to its optimal mechanical properties. The SLA method is known for producing highly detailed and accurate objects with seamless surface finishes. Once the resin is hardened, though, it cannot be recycled. Discarded parts need to be disposed as household waste.

FDM is a widely used, cost-effective 3D printing technology. A thermoplastic filament, in our case, biodegradable, polyactic acid (PLA), is fed into a heated nozzle that melts the material and then precisely extrudes it onto the build platform, constructing the 3D object layer by layer. FDM printing is characterized by the lowest entry and material price of the 3D printing market, by very simple usage, and for having the lowest environmental impact with respect to other 3D printing technologies (Y. Li et al., 2017). The latter is mainly due to its lower process energy consumption and the possibility of reusing or recycling its wasted products. These factors make FDM a highly popular choice for proof of concept purposes and prototyping. However, the level of accuracy and precision that FDM can offer is limited by the diameter of the circular orifice of the nozzle tip (in our case 0.4 mm). In addition, the layer-by-layer deposition (with 0.1 mm of resolution) limits the quality of curved surfaces, causing a grainy surface finishing.

The ability of defining the exact shape, position, orientation, and density of the pore microstructure in a homogeneous matrix makes 3D printing highly attractive for evaluating the predictive capacity and limitations of EMT. In the context of 3D printing for EMT testing purposes, the starting material needs to be as isotropic, non-porous, and homogeneous as possible. Because both SLA and FDM printed objects are built layer by layer, some anisotropy is to be expected in the mechanical properties of printed materials. Mechanical anisotropy has been shown to be low ($\approx$1%) for SLA printed objects (Kazmer, 2017) although it can be affected by the prescribed resolution/layer thickness (Chockalingam et al., 2006). A helium pycnometer was used to measured the connected porosity of our 3D printed cylindrical samples, obtaining a porosity of 1.2% for whole SLA printed samples.

Table 1
Comparison of Features Between SLA and FDM 3D Printing Technologies in the Context of EMT Testing

Feature	SLA	FDM	In favour of
Resolution and accuracy	Higher	Lower	SLA
Surface finishing	Smooth	Not smooth	SLA
Mechanical anisotropy	Lower	Higher	SLA
Porosity	1%	5%	SLA
Post-printing processing	Required	Not required	FDM
Printer and material cost	Higher	Lower	FDM
Environmental impact	Higher	Lower	FDM

By contrast, mechanical anisotropy can be significant for FDM printed samples (Kazmer, 2017). The magnitude of mechanical anisotropy is affected by several printing parameters, which define the drawing pattern to be followed by the nozzle tip. One or more perimeters are first drawn to delimit the object's boundary. Then, the nozzle tip moves back and forth at a prescribed angle (raster angle) to fill the delimited perimeter(s). The prescribed amount of delimiting perimeters, the raster angle, and the layered structured of the samples will determine the mechanical anisotropy of FDM printed samples (Mohamed et al., 2015). To verify the magnitude of anisotropy of FDM printed samples, we performed acoustic velocity measurements on four PLA cubes (30 mm^3) with two perimeters, rectilinear infill—the only recommended pattern for 100% infill—and default other printing specifications. Our results indicated 0.8%–3.3% of anisotropy in the direction orthogonal to layering compared with parallel to layering. This anisotropy can be considered non-significant, hence, isotropic symmetry was assumed in the context of EMT predictions and experimental limitations. Another potential issue is caused by the air gaps between layers and rasters that result in an intrinsic porosity for FDM 3D printed samples of around 5%, as measured by a helium displacement pycnometer. Main aforementioned features of both 3D printing technologies are listed in Table 1.

2.2. Young's Modulus Measurements

The magnitude of Young's modulus may be significantly affected by the selected calculation methodology. Dean et al. (1995) distinguished at least three terms that can be used to specify the Young's modulus value: tangent modulus, chord modulus, and secant modulus. The first term describes a modulus obtained from a tangent line to the stress-strain curve. According to the ASTM standards for compression measurements of rigid plastic materials (ASTM-D695), a tangent line should be constructed at any point in the straight-line part, whereas if there is no clearly linear region, one should construct a tangent to reach the maximum (steepest) slope of the curve. The second term describes a modulus measured as the slope of the line connecting the selected start and end points of the stress-strain curve. Finally, the secant modulus is a particular type of chord modulus, where the start point is defined as the origin of the stress/strain curve.

As reported by Malkowski et al. (2018), based on over two hundred compressed rock samples, Young's moduli values differ significantly based on the choice of modulus computation and of the start and end points for the modulus calculation. For example, they find that the secant modulus measure is inadequate for Young's modulus calculation of sedimentary rocks, and suggest that chord modulus of a narrower range (e.g., 30%–70% of ultimate strength) might be the most suitable measure of Young's moduli.

In this paper, our primary goal is to consider the impact of voids on the effective elastic moduli of materials. Because results might be affected by the selected Young's moduli derivation methodology, we follow a similar approach to that of Malkowski et al. (2018) and compare different Young's moduli computation methods (see Section 3.3) to determine the most suitable approach for calculating Young's Modulus for 3D printed, polymer materials.

2.3. Effective Medium Predictions

In this section, we indicate how the elastic moduli that we measure during uniaxial compression tests are employed to obtain the theoretical effective medium predictions, and we specify how these predictions are calculated.

In a uniaxial compression test, the components of the principal stress tensor can be written as $\sigma_1 \neq 0$, $\sigma_2 = 0$, and $\sigma_3 = 0$. In every test, we measure the axial strain in the direction of compression that—invoking Hooke's law—is equal to $\varepsilon_1 = S_{1111}\sigma_1$, where $S_{ijk\ell}$ denotes the forth-order compliance tensor. Additionally, if a sample is isotropic or transversely isotropic (TI) with the symmetry axis aligned with the compression direction, we measure the radial strain that is equal to $\varepsilon_r = \varepsilon_2 = \varepsilon_3 = S_{1122}\sigma_1$. The above elastic properties can be expressed as Young's modulus and Poisson's ratio, namely, $E := \sigma_1/\varepsilon_1 = 1/S_{1111}$ and $\nu := -\varepsilon_r/\varepsilon_1 = -S_{1122}/S_{1111}$, respectively. In the case of a compression test of a solid sample, both Young's modulus and Poisson's ratio are background moduli

used in the theoretical predictions, as explained later. In the case of a sample with a void (that usually induces anisotropy of lower symmetry than TI), we measure Young's modulus only, which is the effective parameter.

In effective medium theory, it is assumed that a representative volume element (RVE) constitutes a sufficiently large and statistically representative sample of the composite/porous material (Kachanov & Sevostianov, 2018). In addition, the RVE should be small enough not to be influenced by variations in macroscopic forces. If the RVE is defined correctly (Cosenza et al., 2019), the effective properties should be independent of the selected boundary conditions. However, because of experimental restrictions, in some cases our samples are smaller than the RVE. Hence, their effective properties or, as called by Huet (1990), their apparent properties, depend on the boundary conditions. Nevertheless, experiments on samples with volumes smaller than RVE are meaningful, and provide valuable information on effective properties. As proved by Huet (1990), for any volume of averaging, the "apparent" constants provided by the uniform stress and uniform displacement boundary conditions constitute bounds for the effective constants, as explained below.

Effective properties of a medium with a single inhomogeneity (e.g., void) can be predicted differently depending on the boundary conditions we choose. If stress is assumed to be uniform under the absence of the ellipsoidal inhomogeneity, then the findings by Hill (1952) and Eshelby (1957) can be formulated as (Shafiro & Kachanov, 1997),

$$S^{\sigma}_{ijk\ell} = S^0_{ijk\ell} + \phi H_{ijk\ell} + \phi \Delta H_{ijk\ell}, \tag{1}$$

where $S^0_{ijk\ell}$ is the background compliance tensor, ϕ is the inhomogeneity volume fraction, $H_{ijk\ell}$ is the compliance increase due to void presence, and $\Delta H_{ijk\ell}$ is the compliance correction factor due to the presence of fluid or solid in the void. If displacement, not stress, is assumed to be uniform, then

$$S^{\varepsilon}_{ijk\ell} = \left(C^0_{ijk\ell} + \phi N_{ijk\ell} + \phi \Delta N_{ijk\ell} \right)^{-1}, \tag{2}$$

where $C^0_{ijk\ell}$ is the background stiffness tensor, $N_{ijk\ell}$ is the stiffness decrease due to the presence of the void, and $\Delta N_{ijk\ell}$ is the stiffness correction factor due to the presence of fluid or solid in the void. In this paper, we do not consider fluid or solid filling of the void; hence, the last term in Equations 1 and 2 equals zero.

Since, as proved by Huet (1990),

$$S^{\sigma}_{ijkl} \geq S^{\text{eff}}_{ijk\ell} \geq S^{\varepsilon}_{ijk\ell} \tag{3}$$

we can use Equations 1 and 2 to obtain the maximum and minimum predicted values of the effective Young's modulus $1/S^{eff}_{1111}$, respectively. Both expressions give approximately equal values if the void is small because the RVE assumption is satisfied. However, the range of prediction rises with larger ϕ due to the apparent properties measured (RVE smaller than the sample).

$H_{ijk\ell}$ and $N_{ijk\ell}$ can be derived analytically for ellipsoids embedded in an isotropic or TI background. They depend on (a) void shape, (b) void orientation, and (c) background Poisson's ratio. The exact expressions for $H_{ijk\ell}$ and $N_{ijk\ell}$ are presented in Appendix A. Therefore, the range of effective Young's modulus can be predicted if we know the geometry of the void, and we measured Young's modulus and Poisson's ratio of the solid sample, since the same elastic properties are assumed to describe the background of the sample with a void.

In the case of multiple voids, if one assumes that the distance between inhomogeneities is great enough, then the stress at the boundary of each void region is nearly the same as at the boundary of the body. We can write the so-called non-interaction approximation (NIA) as

$$S^{\sigma}_{ijk\ell} = S^0_{ijk\ell} + \sum_m \phi^{(m)} H^{(m)}_{ijk\ell}, \tag{4}$$

where superscript m describes each void in the medium. If the displacement at the boundary of each void region is nearly the same as at the boundary of the body, we get a dual version of NIA,
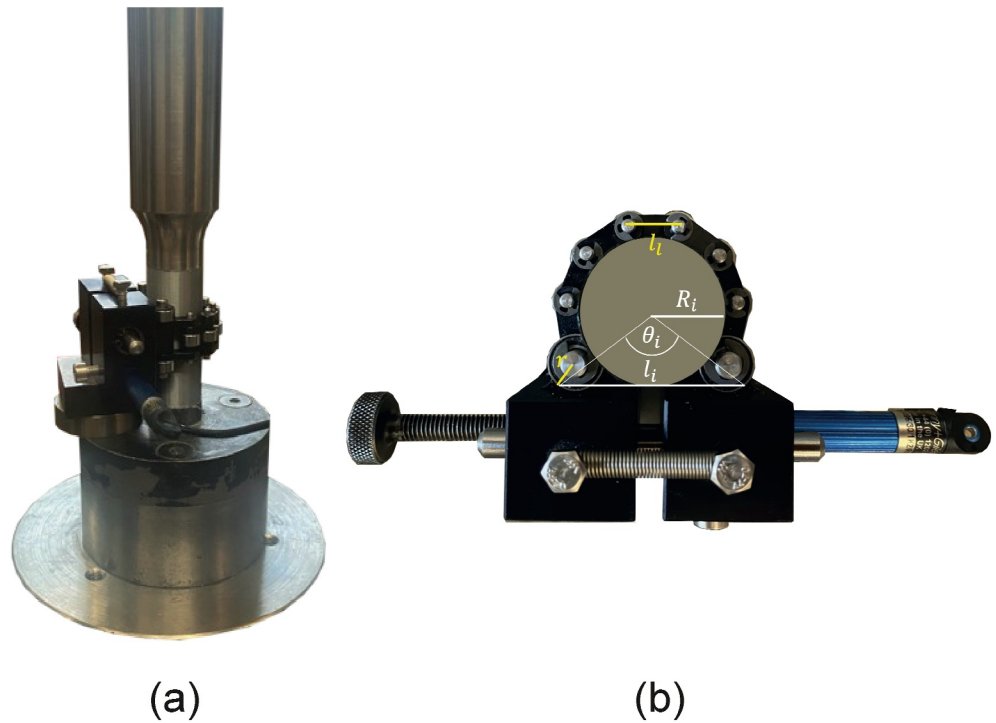
Figure 1. (a) 3D printed sample loaded in the uniaxial frame. (b) Extensometer and parameters to obtain circumferential strain.

$$S_{ijk\ell}^{\varepsilon} = \left(C_{ijk\ell}^{0} + \sum_{m} \phi^{(m)} N_{ijk\ell}^{(m)} \right)^{-1}. \tag{5}$$

In the case where voids are relatively close to each other, the interaction between them may disturb the stress and displacement field. This is why several interaction schemes, such as the self-consistent, differential, Maxwell, or Mori-Tanaka schemes, were proposed (Kachanov, 1992). Nevertheless, all of them use NIA as a building block and predict effective compliances within the range provided by expressions Equations 4 and 5 because these schemes are designed to account for larger concentrations of voids where the interactions effects mostly balance each other. In our case, however, there are few relatively large voids, where local impacts may be more dominant (Kachanov & Sevostianov, 2018). As revised by Kachanov (1992), at local scale, the shielding or amplification effects can lead to smaller or larger softening of the material, respectively. Sevostianov and Kachanov (2010) indicate that these effects are especially noticeable in case of cracks. Co-linear cracks can lead to stronger softening (decreased Young's modulus) as it would be predicted by NIA, whereas stacked cracks lead to weaker softening (increased Young's modulus) as compared to non-interactive estimation. In fact, two stacked cracks, if close to each other, can act as one in terms of the elasticity softening (Kachanov & Sevostianov, 2018). To our best knowledge, there is no universal formula to quantify the shielding/amplification within EMT. In this paper, we compare the experimental results with the range of theoretical predictions from Equations 3 and 4, conscious of NIA limitations. In fact, the discrepancy between NIA and experimental results might indicate the importance and strength of local interaction effects.

3. Experiments

3.1. Experimental Setup: Uniaxial Compression

3D printed samples were subjected to uniaxial compression using a servo-controlled uniaxial load frame in the Rock and Ice Physics Laboratory of University College London (Figure 1a). Samples were loaded at a strain rate
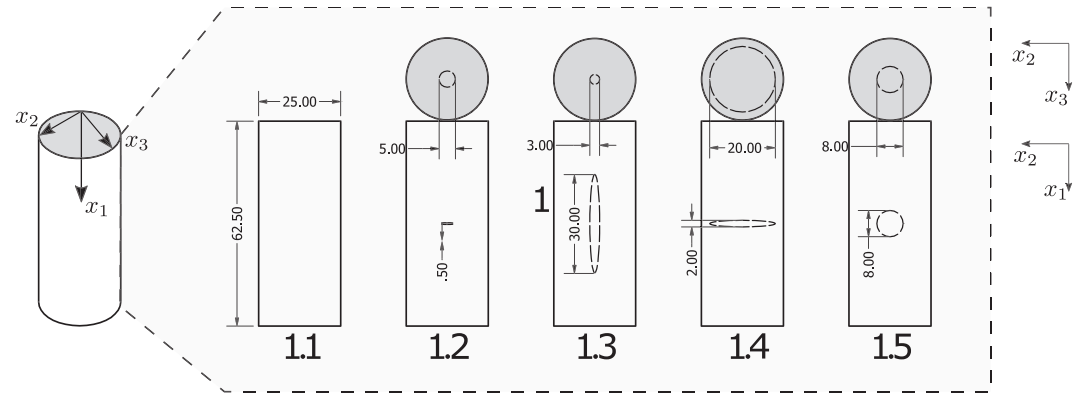
Figure 2. Geometry of samples designed for the preliminary phase of the experiments, where dimensions are in millimeters. Sample 1.1 is solid, whereas samples 1.2 and 1.4 consist of strongly oblate spheres having a 0.1 aspect ratio.

of 10^{-5}s^{-1} until yielding. Strain rate was kept constant and equal for all the experiments to avoid strain-rate sensitivity issues (e.g., viscoelasticity) that are known to affect polymer materials (Z. Li & Lambros, 2001). Axial strain was continuously measured using an external linear variable differential transformer (LVDT) displacement transducer, while load was recorded using a 200 kN load cell. Corrections were applied to the axial displacement data to account for machine stiffness. Intact (solid) 3D printed cores were uniaxially deformed while taking continuous measurements of circumferential strain using an LVDT extensometer (Figure 1b). The correction applied to convert from linear displacement (LVDT output) to circumferential strain is detailed as follows. The initial aperture angle θ_i is obtained from the initial sample radius R_i, the total chain length $l_c = 7l_l$, where l_l is the link length, and extensometer rod radius r from,

$$\theta_i = 2\pi - \frac{l_c}{R_i + r}.$$

(6)

The circumferential strain ϵ_c is calculated from the differential LVDT output $\delta l = l_f - l_i$ (see Figure 1) as,

$$\epsilon_c = \frac{2\pi\delta l}{\sin(\theta_i/2) + \cos(\theta_i/2)(\pi - \theta_i/2)}.$$

(7)

3.2. Samples: Configuration and Preparation

We designed 20 types of cylindrical samples having different configurations of voids. These samples were 62.5 mm long with a diameter of 25 mm. This way, the 2.5 proportion between length and diameter suggested by ASTM-D695 and rock experimentalists (e.g., Paterson & Wong, 2005) is achieved. We divided the samples into two groups designed for two phases of experiments. In the preliminary phase of tests (numbering of samples preceded with 1), we compressed only five types of cores that are either solid or have a single void (samples 1.1–1.5). Their simple configuration allowed us to verify the influence of 3D printer type, specifications (or cure time), and long-crack edge effects on the results (see Section 4.5). Subsequently, in the second phase, we chose the best performing—in the context of measurement/prediction error—3D printer and specification to perform experiments on 15 types of cores having voids with diminished edge effect and more complicated configurations (samples 2.1–2.15). Let us discuss the configuration and preparation of the samples from each group separately.

The longitudinal and cross-sections of samples designed for the preliminary phase of experiments are depicted in Figure 2. Concise description of the voids geometries can be found in Table 2. Sample 1.1 is necessary to obtain the elastic properties of the background material that are used in the theoretical calculations Equations 4 and 5. Theoretically, a void with a very low aspect ratio makes the softening more pronounced, an this effect should be even more significant if the volume of the pore increases. Therefore, samples 1.2 and 1.4 were designed to verify the influence of pore volume along with the possible effects of decreasing the distance between pore boundary and sample edge. Samples 1.3 and 1.5 contain one prolate ellipsoid and one sphere, respectively. The sizes of voids are

Table 2
Description of Samples Designed for the Preliminary Phase of the Experiments

Sample	Void type	Radius [mm]	Aspect ratio	Number of voids	Orientation
1.1	—	—	—	0	—
1.2	Oblate spheroid	2.5	0.1	1	Horizontal
1.3	Prolate spheroid	1.5	10	1	Vertical
1.4	Oblate spheroid	10	0.1	1	Horizontal
1.5	Sphere	4	1	1	—

Note. All voids are placed in the center of the sample.

designed in such a way as to overcome the limitation of printer resolution and make the softening significant enough for it to be easily measurable. The samples were printed using FDM (Prusa i3 MK3S+ printer) and SLA (Form3+ printer) technologies. In the case of FDM printing, we used PLA as the filament material. We set 100% rectilinear infill and select two different options for wall thicknesses (perimeters); our samples have either two or five perimeters. In Figure 4, we present half-printed samples having two perimeters. It can be seen that the low aspect ratio of cracks in samples 1.2 and 1.4 leads to some printing imperfections. Also, the visual effect that the number of perimeters has on the edges of both the sample and the internal void can be appreciated in Figure 3.

In the case of the SLA printing, we used standard grey resin. The manufacturer suggests putting freshly printed material in IPA (alcohol) and heating it to make the fabric stiffer. In this paper, we go beyond this suggestion and check two other procedures: (a) IPA cleaning and cure for a month without heating, (b) IPA cleaning and cure for a week without heating, and (c) IPA cleaning, heating (60°C), and fast cure (between 4 hr and 2 days). This way, we verify the influence of a cure time on the sample stiffness and compare it with the influence of the heating. In Figure 5, we present cleaned SLA samples cut in half. While cutting them, we noticed the remaining residual resin inside the voids that may have an influence on sample stiffness, as shown in Figure 6.

The longitudinal and cross-sections of samples designed for the final phase of experiments are depicted in Figure 7; the concise description of voids' geometries can be found in Table 3. Samples 2.1 and 2.2 contain a sphere and a prolate spheroid, respectively. They are similar to samples 1.5 and 1.3, but the volume fraction of the voids is larger to augment the softening effect. In the remaining samples, 2.3–2.15, we focus on crack-like shapes that are crucial in the context of for example, geomaterials. These samples consist of either isolated, overlapping, or crossing oblate spheroids having a 0.2 aspect ratio and radius of 8 mm. The radius of the voids is smaller than

25 mm
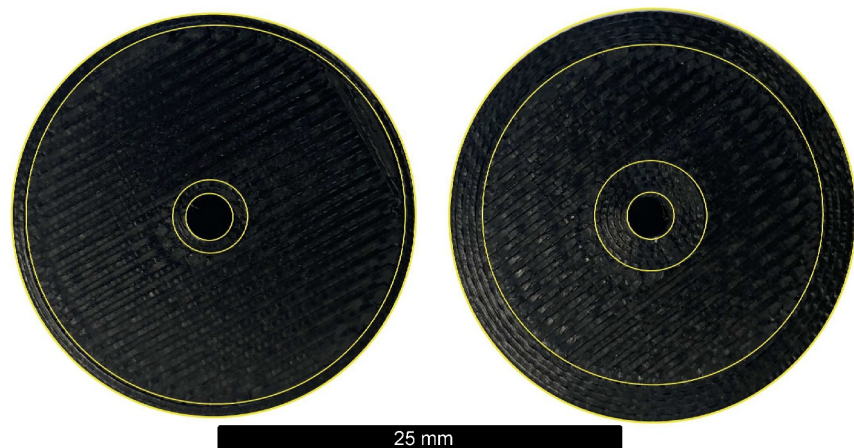
Figure 3. Difference of prescribed perimeters (two in the left, five to the right) on the final structure of porous samples printed with the FDM technology. The thickness of the perimeters delimiting the samples and the pores edges are highlighted in yellow, showing that for an equal size pore, the prescription of five printing perimeter results in a significantly thicker, concentric boundary that affects the internal microstructure of the sample.
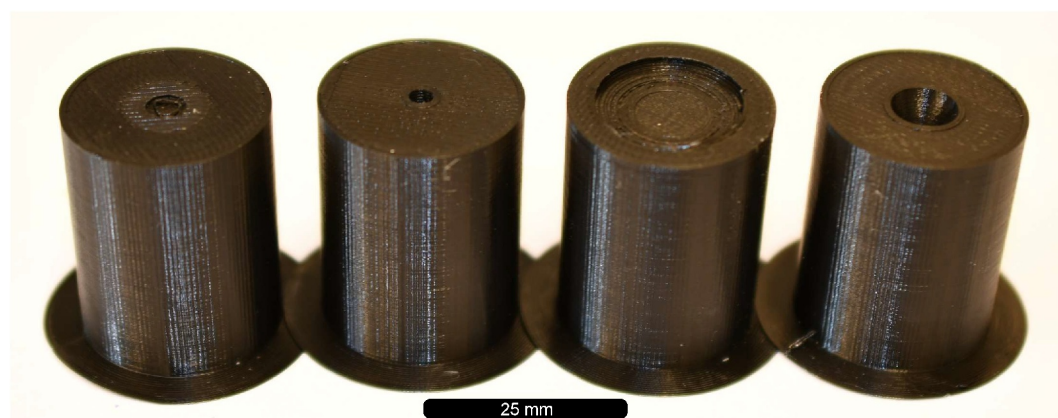
Figure 4. Half-printed FDM samples having two perimeters used in the preliminary phase of experiments. Samples have brims that prevent their detachment from the bed.

that of sample 1.4; this way, the edge effect is diminished and potential collapse of the crack is inhibited. By contrast, the aspect ratio is augmented to (a) avoid printing imperfections, (b) keep a significant softening effect, (c) keep it flat enough to be considered a crack, and (d) allow fluid injection in the future. Samples 2.3 and 2.4 are designed to verify the influence of a crack-like void orientation. We designed other samples to verify the possible influence of interactions between two vertical cracks (samples 2.5 and 2.8), horizontal cracks (samples 2.6 and 2.9), and vertical and horizontal cracks (samples 2.7, 2.10, and 2.11). Further, samples 2.12–2.15 may allow us to measure the significant softening effect (as compared to solid sample 1.1) and interaction influence of a moderate crack concentration; the total volume fraction of voids in samples 2.12–2.13 is $\phi \approx 5.6\%$ and in samples 2.14–2.15 is $\phi \approx 11.2\%$. Note that the overlapping of the samples is small enough to keep the crack-like shapes but perhaps sufficient to equilibrate pore pressure in future fluid injection experiments. In this phase of experiments, all samples are printed using FDM technology and have two perimeters. The interior of each void (either isolated, overlapping, or crossing) type is shown in Figure 8.

3.3. Moduli Definitions and Measurement Repetitions

As mentioned in Section 2.3, we measured either Young's modulus and Poisson's ratio (solid samples) or Young's modulus only (samples with voids). We calculated Young's modulus from the slope of the following portions of the strain-stress curve:
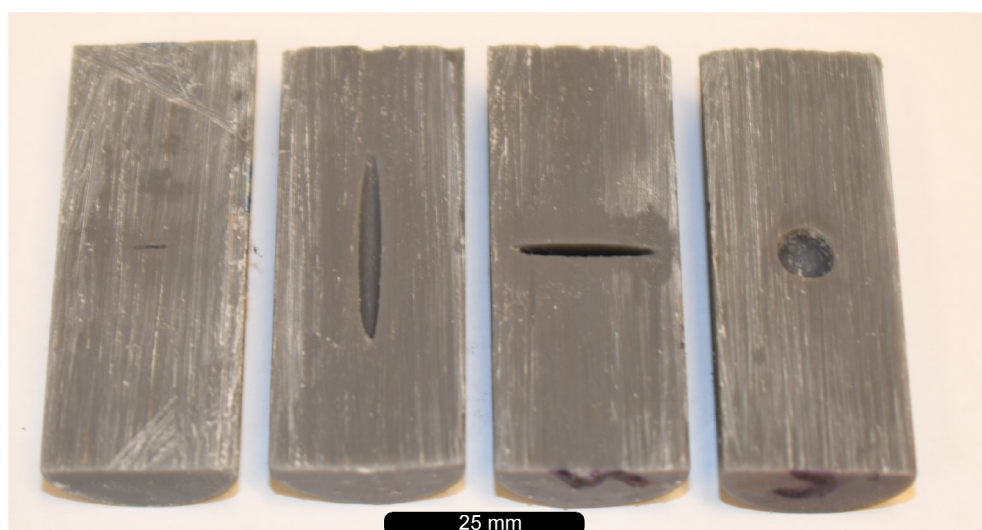

Figure 5. Printed and deformed SLA samples cut in half with voids cleaned.
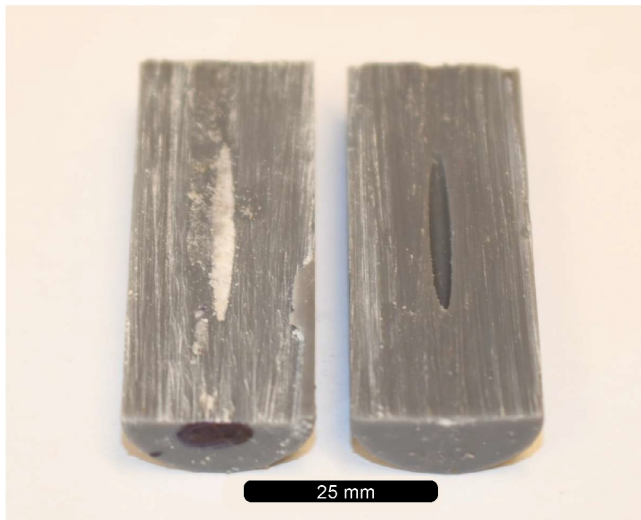
Figure 6. Residual resin present in the uncleaned void of an SLA printed sample.

- 15% and 30% of the yield strength, E_{15-30},
- 25% and 50% of the yield strength, E_{25-50},
- 25% and 75% of the yield strength, E_{25-75},
- Lower and upper elastic limits, E_{el}.

In the case of FDM, the yield strength (σ_y) was determined based on the first peak of the stress-strain curve. In the case of SLA, σ_y is difficult to determine unequivocally due to the continuous growth of stress with displacement. Therefore, we arbitrarily chose a threshold of 6% strain to obtain the reference point (yield strength approximation) used to calculate the limits of Young's modulus. To define the Poisson's ratio, we first estimated two ranges of stresses that correspond to the elastic part of the axial and radial strain curves. Second, we chose a common range of stress that—in a set theory sense—is the intersection of the two aforementioned ranges. This way, the parts of ε_1 and ε_r needed for Poisson's ratio computation are unequivocally determined.

Our compression experiments and modulus measurements are less prone to random errors due to the repetitions of 3D printing and testing of identically designed samples. This way, more reliable average values of moduli can be obtained. Table 4 lists the number of repetitions of valid measurements for each sample type of this study. Note that the solid sample (1.1) has the most repetitions; this is due to its importance for the EMT calculations.

4. Results

4.1. Stress-Strain Curves

Results of axial strain as a function of stress are plotted for the five preliminary-phase microstructural configurations (samples 1.1–1.5) (Figure 9). Selected curves are plotted for (a) FDM printed samples with 2 perimeters (FDM$_t$), (b) FDM printed samples with 5 perimeters (FDM$_v$), (c) SLA printed samples tested after month of post-printing curing time at room temperature (SLA$_m$), (d) SLA after a week of curing time at ambient temperature (SLA$_w$) and (e) SLA after curing in a heated chamber at 60°C for 1 hr, and then post-curing at ambient temperature for a minimum time of 4 hr and a maximum of 2 days (SLA$_f$). Curves are plotted up to their yield points, displaying their elastic ranges and the portions of the curves considered for elasticity modulus computation. Circumferential strain as a function of stress is plotted for a solid FDM$_t$ sample, displaying the ranges considered for Poisson's ratio determination.

It can be seen that FDM printed samples are stiffer and stonger with respect to SLA samples, and that the printing pattern (numbers of delimiting perimeters) does not significantly affect their mechanical behavior, although samples printed with two perimeters (FDM$_t$) consistently display higher stiffness and higher yield strength with respect to those with five delimiting contours (FDM$_v$) for all preliminary-phase samples except for 1.4. SLA printed samples are relatively soft, elasto-plastic materials. Curing time and method have a significant influence on the mechanical properties of SLA printed samples. Two days of curing time within a heated chamber at 60°C is shown to be the most effective method to drive the material to higher mechanical strength. In addition, samples cured for 1 month are consistently stiffer and stronger than samples cured for 1 week.

The microstructural configuration of samples does not significantly affect the mechanical properties of preliminary-phase 3D printed samples, except for the 1.4 microstructural design, which notably alters the deformation mechanism of FDM printed samples. This design has the largest void fraction and smallest distance from void to sample edge. Predictably, this microstructural configuration induces a significant softening effect and causes a different deformation mechanism by which the pore boundaries collapse at lower stress due to stress concentrations at the thin walls surrounding the pore (Figure 10).

Poisson's ratio measurements for solid FDM samples printed with two and five perimeters (FDM$_t$, FDM$_v$) and SLA samples with the previously described curing methods (SLA$_m$, SLA$_w$, SLA$_f$) are indicated in Table 5.
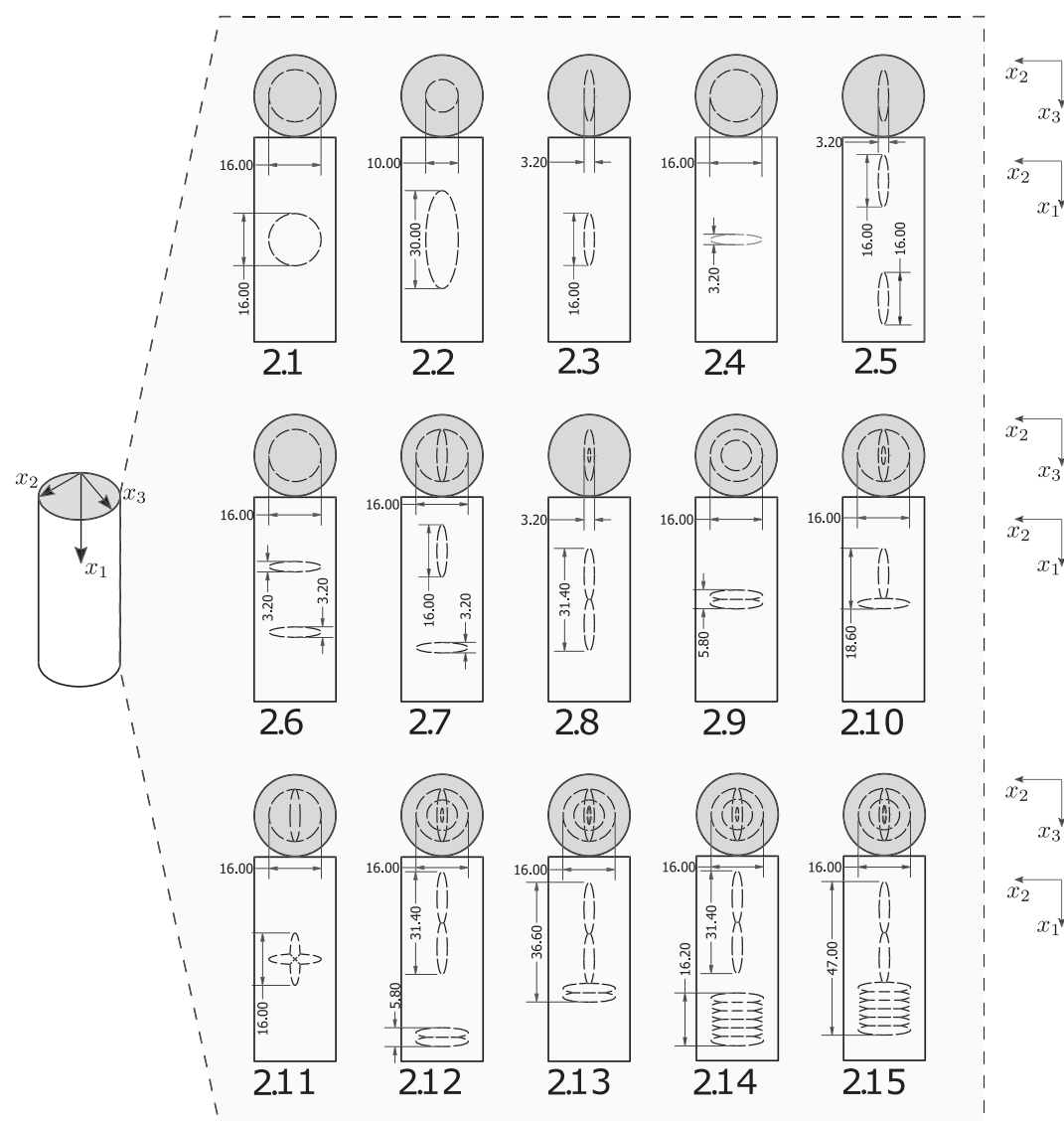
Figure 7. Geometry of samples designed for the final phase of experiments, where dimensions are in millimetres. Samples 2.3–2.15 consist of either isolated, overlapping, or crossing oblate spheroids having a 0.2 aspect ratio and 8 mm of radius.

4.2. Mean Young's Modulus of Solid FDM Samples

The average Young's modulus calculated from the arithmetic mean of 12 and 6 repeated tests for solid FDM samples, and samples 1.2–1.5, respectively, are shown in Figure 11 and listed in Table 6 for the four modulus determination methods described in Section 2.2. Young's modulus of solid samples consistently lie between 2.6 and 2.7GPa, and display a scatter of ±0.2GPa, in accordance with magnitudes reported in the literature (Dizon et al., 2018). Results do not follow a Gaussian distribution, although this is likely due to insufficient number of tested samples. These results highlight the need for considering means calculated from a significant statistical sample size to obtain meaningful and representative results for the elasticity modulus of 3D printed samples.

Young's modulus results vary depending on the portion of the elastic range chosen for modulus computation. The higher magnitudes are obtained using the 25 to 50% portion of the elastic range. FDM_t samples display a consistently higher Young's modulus with respect to FDM_v, although the difference is not significant (0.05GPa or less).

Table 3
Description of Samples Designed for the Final Phase of Experiments

Sample	Void type(s)	Number of voids	Void center to sample center [mm]	Orientation(s)
2.1	Sphere, $a = 8$ mm	1	0	—
2.2	Prolate spheroid $a = 5$ mm, $\gamma = 3$	1	0	vrt.
2.3	Oblate spheroid	1	0	vert.
2.4	Oblate spheroid	1	0	hor.
2.5	Oblate spheroids	2	18/−18	vrt./vrt.
2.6	Oblate spheroids	2	11.6/−11.6	hor./hor.
2.7	Oblate spheroids	2	14.8/−14.8	vrt./hor.
2.8	Oblate spheroids	2	7.7/−7.7	vrt./vrt.
2.9	Oblate spheroids	2	1.3/−1.3	hor./hor.
2.10	Oblate spheroids	2	7.7/−1.3	vrt./hor.
2.11	Oblate spheroids	2	0/0	vrt./hor.
2.12	Oblate spheroids	4	18.75/3.35/−22.55/−25.15	vrt./vrt./hor./hor.
2.13	Oblate spheroids	4	15.4/0/−9/−11.6	vrt./vrt./hor./hor.
2.14	Oblate spheroids	8	18.75/3.35/−12.15/−14.75/ −17.35/−19.95/−22.55/−25.15	vrt.x2/hor.x6
2.15	Oblate spheroids	8	15.5/0.1/−8.9/−11.5/ −14.1/−16.7/−19.3/−21.9	vrt.x2/hor.x6

Note. All voids are centered horizontally. The distance measured from the void center towards the bottom of the sample is positive. Orientations of the voids are listed in descending order starting from the uppermost void. All oblate spheroids have a radius $a = 8$ mm and aspect ratio $\gamma = 0.2$.

4.3. Effect of Post-Printing Curing Methods for the Mechanical Behaviour of SLA Samples

Samples 1.1–1.5 were printed using the SLA method and treated with the curing procedures described in Section 4.1 (1 month at room temperature, 1 week at room temperature, 1 hr in 60°C chamber). Three series of samples 1.1–1.5 were printed, treated, and tested for each curing method. Two additional series of samples were tested immediately after heating (no curing time). This workflow was followed to evaluate the repeatability of results for printed samples following the same post-printing processing. Calculations of E_{25-50} for the different series processed using the same method, for each curing procedure, are displayed in Figure 12. The Young's modulus (E_{25-50}) axis ranges are set purposely to allow visualization of the scatter of results between different series. The scatter in E_{25-50} is overall is below 0.2 GPa (equivalent to 20% of the mean effective modulus). However, there is a consistent trend in the magnitude of Young's modulus between series. For example, series 2 of 1 month-cured samples have consistently higher E_{25-50} magnitudes for all 1.1–1.5 samples with respect to series 1 and 3, which were subjected to equal post-printing procedures. Similar trends are observed for all curing methods, indicating a clear influence of printing batch on the resulting mechanical properties. This observation highlights the difficulty of repeatability for SLA printed samples, even after following the same post-processing procedures.

The effect of the elapsed time between the curing of whole SLA samples and the execution of the uniaxial test to determine the mechanical properties of SLA samples is displayed in Figure 13 for samples that were printed, cured in a 60°C chamber, and tested after 15 min to 2.5 hr. It can be seen that the elapsed time between heating and conducting the deformation experiments correlates positively with stiffness, that is, allowing the samples to cool has a hardening effect on SLA printed samples.

4.4. Elastic and Inelastic Ranges for FDM and SLA Samples

Figure 14 displays results from the strain-curves from tests on preliminary phase FDM and SLA printed samples split into the average percentages of the lower inelastic phase (origin to lower elastic limit), elastic phase (lower to
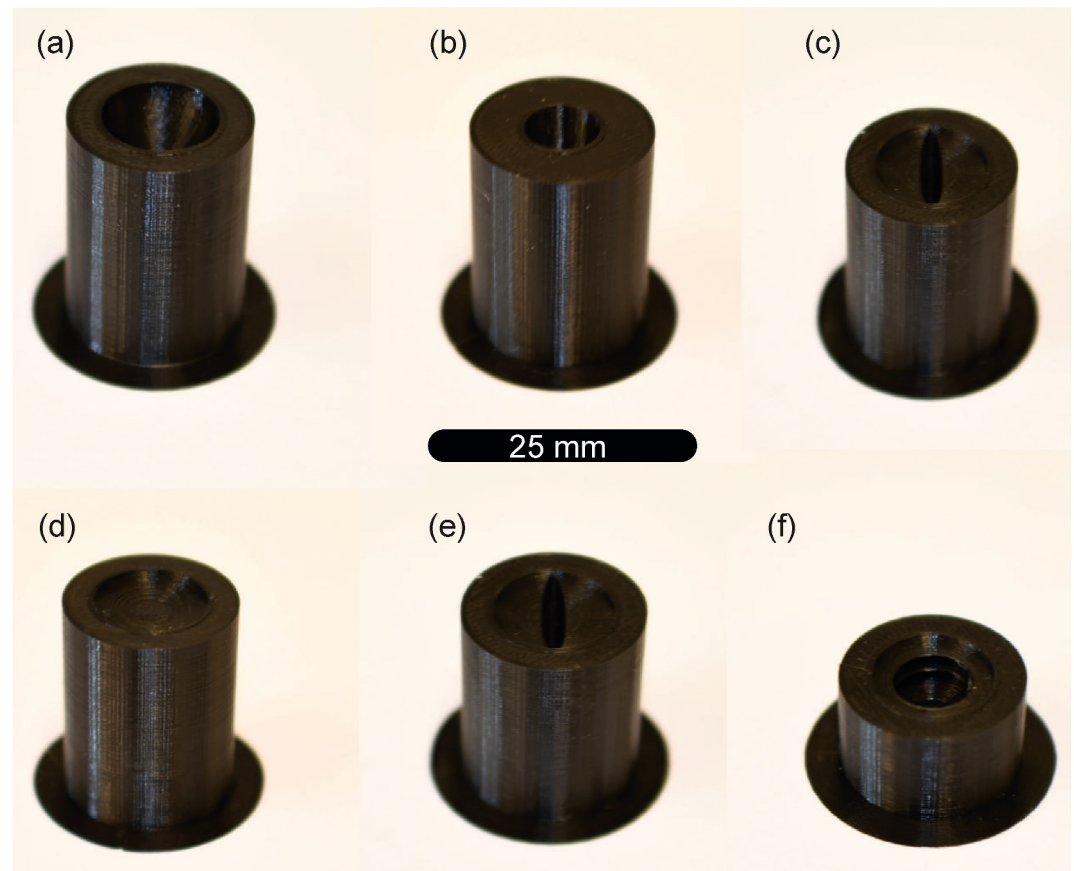
Figure 8. Half-printed FDM samples having two perimeters, used in the final phase of experiments. Each type of printed void is shown. These configurations are present in (a) sample 2.1, (b) sample 2.2, (c) samples 2.3, 2.5, 2.7, 2.8, 2.10, 2.12–2.15, (d) samples 2.4, 2.6, 2.7, 2.9, 2.10, 2.12–2.15, (e) sample 2.11, and (f) samples 2.14–2.15. All cores have brims that prevent their detachment from the bed.

upper elastic limits) and the upper inelastic phase (upper elastic limit to yield point). FDM samples deform elastically over a wider range of stress, with an average of 61.7% of the stress-strain curves. This average is significantly decreased by sample 1.4, which displays a much smaller elastic range due to the different deformation mechanism driven by the pore space collapse. Average elastic ranges for the secondary phase of FDM printed samples (Figure 15) are likely more representative of the mechanical behavior of FDM samples, as none of them displays pore space collapse. They display an average elastic range of 72.4% of the total stress-strain curve.

By contrast, SLA printed samples experience a consistent, albeit smaller, elastic range of 49.3%. The microstructural configuration of sample 1.4 does not produce deformation due to pore space collapse in SLA printed

Table 4
Number of Repetitions of Valid Young's Moduli and Poisson's Ratio Measurements for Each Sample Type

	YM valid measurements			PR valid measurements
	Sample 1.1	Sample 1.2–1.5	Sample 2.1–2.15	Sample 1.1
FDM$_t$ (two perim.)	12	6	6	5
FDM$_v$ (five perim.)	12	6	—	4
SLA$_m$ (month cure)	3	3	—	3
SLA$_w$ (week cure)	3	3	—	3
SLA$_f$ (fast cure, heated)	3	3	—	3
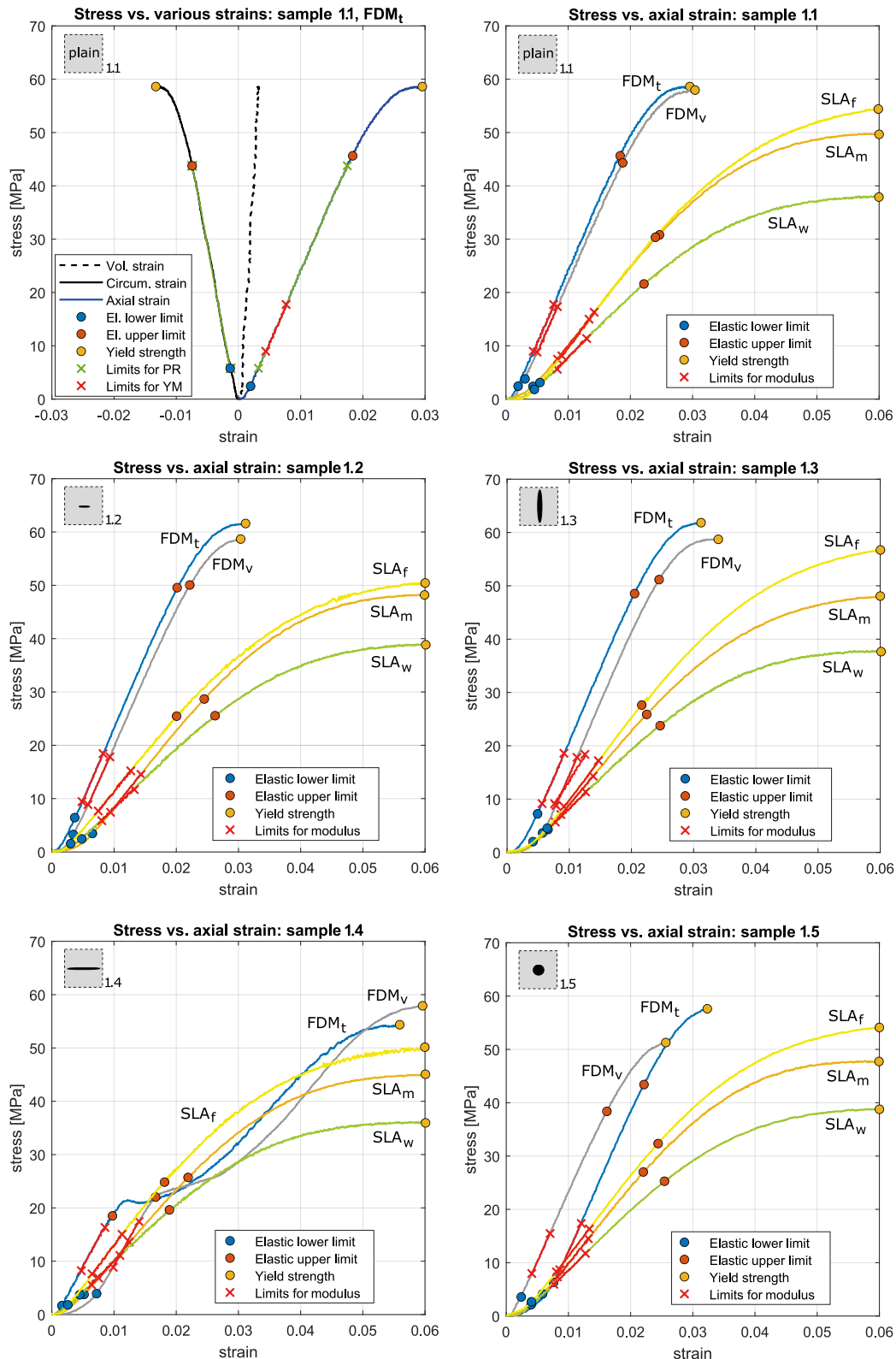
Figure 9. Selected stress-strain curves for samples 1.1–1.5 that are FDM with two perimeters (FDM$_t$) or five perimeters (FDM$_v$), SLA cured for a month (SLA$_m$), a week (SLA$_w$), or heated and fast-cured for less than 2 days (SLA$_f$). Elastic parts, yield points and the range of curve to obtain E_{15-30} are presented. Additionally, the left-upper figure presents the circumferential and volumetric strains of solid FDM sample having two perimeters (FDM$_t$). The Poisson's ratio is obtained based on the elastic portion of the circumferential strain that lies within elastic part of the axial strain.

Figure 10. Inelastic deformation mechanism due to pore space collapse in FDM printed sample with a large oblate pore (1.4).

samples. However, it is important to note that the yield point for SLA printed samples is less well defined. To avoid arbitrary definitions, the yield point of SLA samples was assumed to correspond to 6% of axial strain, throughout.

4.5. Prediction Range From EMT Using Solid Samples Results

Now that we have confidently determined the elastic properties of solid SLA and FDM printed samples (Section 4.2), we can use these results to compute the predicted effective modulus for each sample with voids. However, EMT predictions may not be unequivocal; as they depend on the boundary conditions chosen for theoretical calculations (uniform stress or uniform strain). As a result, for certain pore geometries, different boundary conditions can result in different predicted magnitudes for equal void configurations. In such cases, the prediction of effective Young's modulus from EMT is a range, and not a single magnitude. Herein, we describe the effect that pore space volume and shape have on the range of predictions by EMT. Theoretically, the larger the softening effect caused by a void, the larger the range of estimation is– meaning that the prediction becomes equivocal and, hence, less accurate. Both the softening effect and the prediction range are affected by the interplay of the void's orientation, shape, and size. For the sake of analysis, let us assume a single, horizontal, oblate void, such as those embedded in samples 1.2, 1.4, and 2.4, within a FDM printed sample with two perimeters (FDM$_t$, $E_0 = 2.69$ GPa, and Poisson's ratio of $\nu_0 = 0.41$). If we consider a fixed shape of the horizontal spheroidal void and we increase its radius (e.g., samples 1.2 and 1.4), then the increased volume of the void leads to higher inaccuracy of EMT prediction (Figure 16). By contrast, in the case of a fixed volume of the horizontal void (e.g., samples 2.4 and 1.4), the EMT inaccuracy is affected by the aspect ratio of the spheroid; the lower the aspect ratio, the higher the inaccuracy.

4.6. Comparison With Predictions From Effective Medium Theory

The measured effective elastic modulus of 3D printed samples, considering four different ranges for elasticity modulus computation (E_{15-30}, E_{25-50}, E_{25-75} and the whole elastic portion of the curves), are plotted along with the predicted range for effective Young's modulus calculated from EMT for each microstructral configuration for (a) FDM, preliminary phase printed samples (Figure 17), (b) SLA, preliminary phase printed samples (Figure 18), and (c) secondary phase, FDM printed samples (Figure 19). Details of the plotted values and the computed error of experimental results with respect to EMT predictions are listed in Tables B1–B3 in Appendix B. The error between measured and predicted values was calculated as follows:

$$|R| = \frac{|E_{\text{predicted}} - E_{\text{measured}}|}{|E_{\text{predicted}}|} \times 100\% \tag{8}$$

where E_{measured} is the average effective Young's modulus (averaged over a number of repetitions), and $E_{\text{predicted}}$ is the middle value within the EMT prediction range.

The results of effective Young's modulus for FDM secondary phase samples correspond to the arithmetic mean of six tested samples per sample type, and are plotted normalized with respect to the measured Young's modulus of solid cores. The best fit to EMT predictions is achieved for effective moduli computed with E_{15-30}, and for samples printed with two perimeters, which display very small errors of 0.94%, 0.23%, and 1.08% for samples 1.2, 1.3, and 1.5, respectively. The mismatch between measurements and predictions is highest for sample 1.4 (deformed due to pore space collapse) for any printing set-up and modulus calculation. Measured effective modulus for samples 1.4 are between 5.95% and 65.6% lower than EMT predictions.

The details of computed effective Young's modulus and comparison with EMT predictions for SLA printed samples are displayed in Table B2 and Figure 18. Results are shown for each curing method (1 month cure SLA$_m$,

Table 5
Poisson's Ratio for Solid FDM and SLA Samples

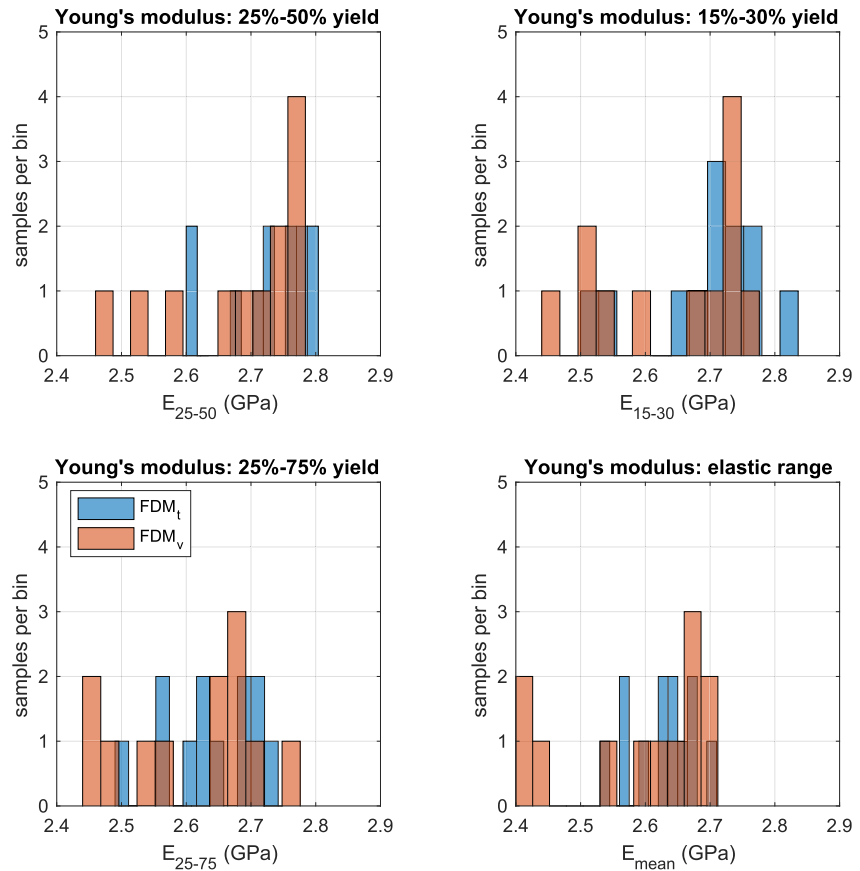| FDM$_t$	FDM$_v$	SLA$_m$	SLA$_w$	SLA$_f$
$\nu_0 = 0.41$	$\nu_0 = 0.38$	$\nu_0 = 0.42$	$\nu_0 = 0.42$	$\nu_0 = 0.45$

Figure 11. Distributions of experimentally obtained Young's modulus for solid FDM samples having either two (FDM$_t$) or five (FDM$_v$) perimeters. In total, there were 24 samples tested. Results in each chart are grouped into 12 bins.

1 week cure SLA$_w$, fast and heated cure SLA$_f$) and for different portions of the elastic curve used for modulus computation. The closest results in terms of matching EMT predictions are achieved with 1 month cured samples (SLA$_m$). The misfit between measurements and predictions are 1.06%, 0.55% and 0.39% for samples 1.2, 1.3, and 1.5, respectively, using E_{15-30} from the stress versus strain curves. Higher errors are consistently observed for sample 1.4, with a mismatch ranging between 11.3% and 22.4%. In contrast to FDM samples, EMT predictions underestimate the effective modulus for this microstructural arrangement with respect to measurements on SLA printed samples.

Comparisons between EMT prediction with respect to measured effective moduli for secondary phase FDM printed samples (Figure 19, Table 3) reveal that, as previously observed, lower mismatches between measurements and predictions are obtained using the E_{15-30} range of the stress versus strain curve, although results are not significantly affected by the modulus computation method. Overall, the best fits to predictions (error below 5%) are obtained for samples with simple microstructural arrangements (either one or two pores) and with lower pore volume fraction (below 3%), which is the case for samples 2.3–2.11. The effective Young's modulus for sample 2.2 (prolate pore, 5.12% porosity) is consistently underestimated by EMT predictions by 9%–10%. By contrast, EMT overestimates the effective modulus of sample 7 (1 oblate plus 1 prolate pore) with respect to measurements, by 4%–9%. The effective modulus for two overlapping oblate pores (sample 9) is underestimated by EMT predictions by 7%–9.5%. Its value is generally similar to

Table 6
Experimentally Obtained Young's Modulus for Solid FDM Samples Having Either Two (Sample 1.1$_t$, Twelve Tests) or Five Perimeters (Sample 1.1$_v$, Twelve Tests)

		1.1$_t$	1.1$_v$	1.1$_t$ & 1.1$_v$
E_{15-30}	Mean	2.69	2.64	2.67
	Range	2.52–2.83	2.44–2.77	2.44–2.83
E_{25-50}	Mean	2.73	2.68	2.71
	Range	2.61–2.79	2.46–2.77	2.46–2.79
E_{25-75}	Mean	2.64	2.61	2.62
	Range	2.50–2.73	2.44–2.77	2.44–2.77
E_{el}	Mean	2.63	2.59	2.61
	Range	2.54–2.70	2.41–2.70	2.41–2.70

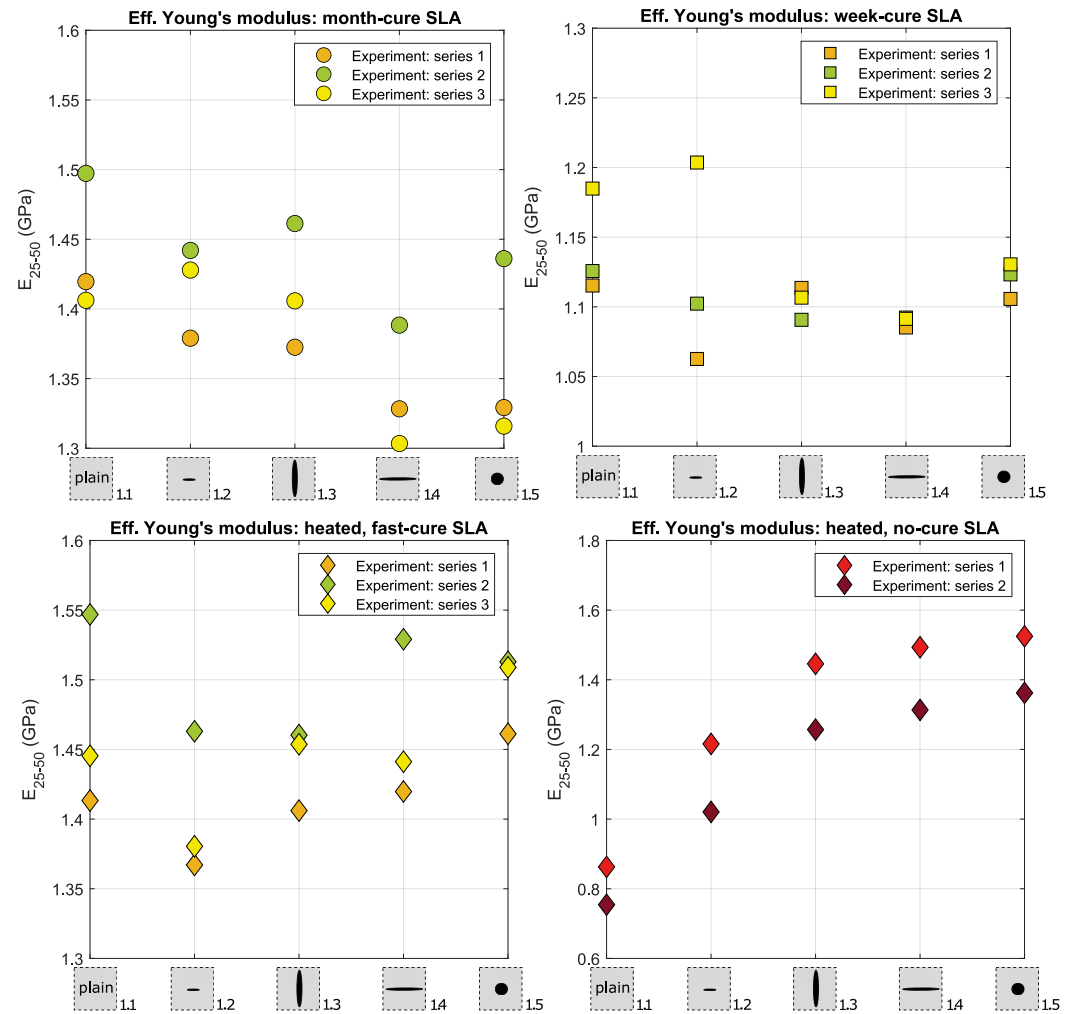*Note.* Mean values and ranges of differently defined modulus are given.

Figure 12. Effective Young's moduli obtained from compression tests of SLA samples. They were printed in a series of five samples 1.1–1.5. Cores were cured for a month, week, were heated with a short cure (between 4 hr and 2 days) or almost no cure. The results show that series differ from each other, and particular printing sessions may affect the stiffness of samples.

effective modulus for sample 4, where only one horizontal oblate pore is present. On the other hand, sample 6 (two horizontal oblate pores further from each other) is well predicted by EMT—the softening effect is stronger as compared to samples 4 and 9.

More complex pore arrangements such as those constituting the internal structure of samples 2.12–2.15 display the highest errors between measurements and predictions. The higher pore fraction volume of these samples causes a larger softening effect, which results in a wider prediction range from EMT. Effective modulus measurements for samples 2.12 and 2.13 ($\phi \approx 5.6\%$) lie 6%–11.4% above the upper limit of the effective modulus range predicted by EMT. By contrast, measured moduli for samples 2.14 and 2.15 ($\phi \approx 11.2\%$) lie approximately 150% above the upper bound of the predicted range.

5. Discussion

We have produced and subjected to uniaxial compression over two hundred 3D printed samples using two different printing technologies, considering distinct printing specifications and post-printing processing methods, and 20 different microstructural configurations. This thorough approach allows us to confidently state
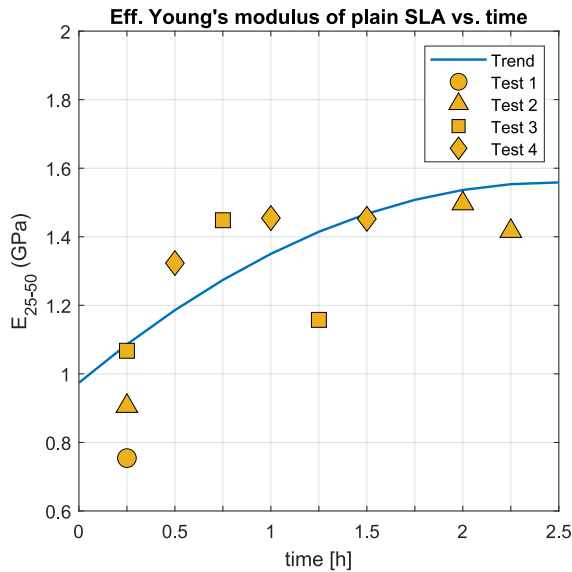
Figure 13. Effect of a cure time of heated samples. Decreasing temperature leads to the stiffening of the samples.

the strengths and limitations of 3D printing to emulate solids with relatively large voids and the capacity of effective medium theory to predict their effective elastic properties. We first discuss the methods and practices that we have seen to optimize the fit of measured elastic moduli with EMT predictions. We then examine the constraints on sample dimension and microstructural design that need to be considered for manufacturing representative porous media.

5.1. 3D Printing Methods and Practices for Best Fit to EMT Predictions

The best fit between measured and predicted elasticity moduli for FDM printed samples (error less than 5%, Table B1) were obtained by specifying two contour perimeters, and by computing Young's modulus using 15%–30% of the stress/strain curve. Our results suggest that the inherent anisotropy in the background medium produced by the printing method (depositional layering, raster angle), the inter-layer porosity, and the limited resolution of the printing method, does not impact significantly on the capacity of FDM samples to emulate a solid medium with voids, when sample design considerations are taken into account (see the following section).

SLA printed samples can also be used to produce controlled porous media. The best fit of measured effective elastic properties with respect to EMT predictions (error below 1%, Table B2) is achieved by curing the printed samples for extended periods (1 month in our case), and by considering E_{15-30} (as above). Successful results using SLA printing methods to match EMT predictions were also obtained by Zerhouni et al. (2019). Importantly, though, our results indicate that repeatability using SLA printed samples is more difficult to achieve. The mechanical properties of SLA samples appear to be affected by uncontrolled factors (e.g., ambient temperature) that cause slightly different results between printed batches, even if subjected to equal post-printing processing. In consequence, meaningful comparisons between elastic properties of SLA cores should always be done on samples printed in the same batch.

We can conclude that both FDM and SLA methods can be used to emulate representative solids with a controlled void space whose effective elastic properties can be predicted by EMT. However, the need for long curing times

Figure 14. Elastic and inelastic parts (in percentages) of an average curve of each FDM and SLA sample type, where the curve ends at the yield strength. In the case of FDM, the yield is determined based on the flat part of the curve. In the case of SLA, yield is difficult to determine; hence, it is assumed to correspond to 6% of strain. For FDM, on average, the elastic part takes 61.7% of the curve. For SLA, on average, the elastic part takes 49.3% of the curve.
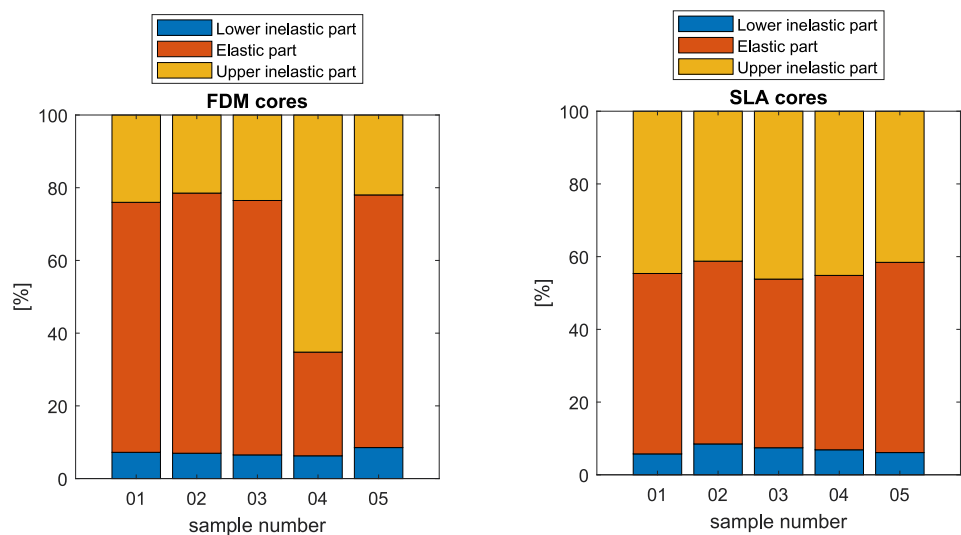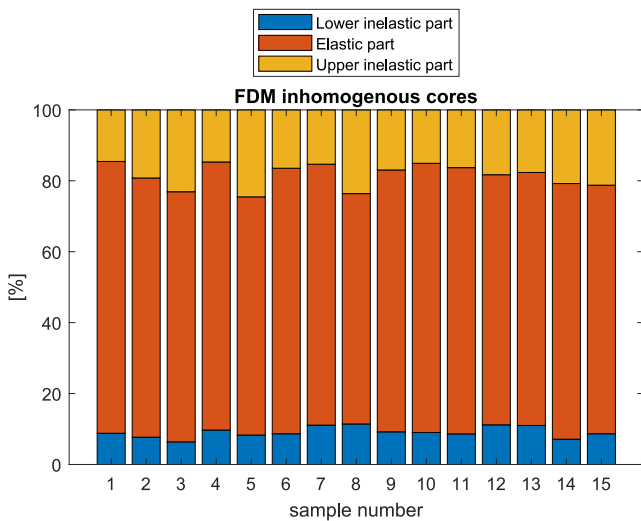
Figure 15. Elastic and inelastic parts (in percentages) of an average curve of each FDM secondary phase sample, where the curve ends at the yield strength. On average, the elastic part takes 72.4% of the curve.

of SLA samples, along with the difficulty of repeatability, added to the higher cost of this technology and the impossibility of recycling its wasted products, makes FDM a more convenient and equally effective method for this purpose.

It is important to note that the porous microstructure of 3D-printed samples is constrained by the printing resolution (0.1 mm), which limits the minimum achievable aspect ratio of ellipsoidal pores to 0.01. In contrast, penny-shaped cracks with lower aspect ratios (≈ 0.001) are typically used to theoretically model microcracked media but cannot be reproduced with current 3D printing technologies. This limitation prevents 3D printing from accurately emulating cracked media. However, the ellipsoidal pores with higher aspect ratios and spherical voids produced in this study effectively represent the microstructure of naturally porous materials, particularly porous rocks. As a result, 3D printing remains a valuable tool for simulating porous media.

5.2. Considerations for Microstructural Design: Pore Volume Fraction and Edge Effect

In order to produce 3D printed samples of an homogeneous medium with voids that can be significantly compared to predictions from EMT, some considerations need to be taken into account. First, the pore volume fraction needs to be sufficient to induce a measurable softening effect, but, at the same time, too large pore volume fraction results in an equivocal, wide range of estimation by EMT that fails to predict the measured effective moduli of samples.

We observe that, for a pore fraction of $\phi \approx 5.6\%$, such as that prescribed for samples 2.12 and 2.13, the range of effective moduli estimations from EMT becomes too wide, and lie below the measured effective properties of 3D printed samples. Results become extremely inaccurate for a pore volume fraction of $\phi \approx 11.2\%$ (samples 2.14, 2.15) with errors above 150% (Table B3). These discrepancies above the upper bound might come from strong shielding effect due to stacked horizontal oblate pores. Interestingly, measured effective moduli are relatively similar to effective Young's modulus for sample 2.6, where only two horizontal oblate but distant pores are present. This may emphasize the importance of distance between horizontal crack-like pores.
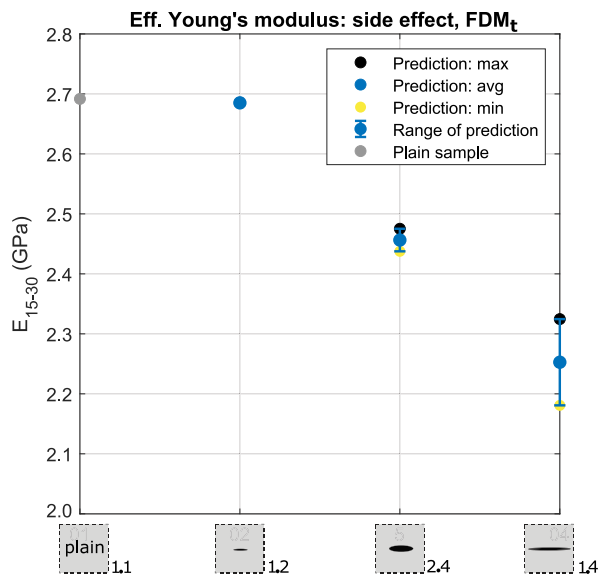
More detailed comparisons can be made between samples with a single pore, equal shape and orientation, but different pore volume fractions. Samples 1.3 and 2.2 both contain a single, prolate, vertical pore, but with pore volume fractions of $\phi = 0.46\%$ and $\phi = 5.12\%$. The misfit between measurements and EMT predictions were 0.23% and 9.34%, respectively. The effect of increased pore volume is smaller when pores are spherical. Sample 1.5 ($\phi = 0.87\%$) displayed a prediction error of 1% whereas sample 2.1 ($\phi = 7\%$) had a 2.4% error with respect to predictions. Samples 1.2, 1.4, and 2.4 all contain a single, horizontal, oblate pore but with volume fractions of $\phi = 0.02\%$, $\phi = 1.4\%$, $\phi = 1.4\%$, the latter with an aspect ratio of 0.2 as opposed to 0.1. The best fit to predictions was obtained for the smaller pore (error of 0.94%), while samples 1.4 and 2.4 displayed errors of 8% and 6%, respectively.

From these results, it is tempting to conclude that smaller pore volume fractions allow EMT to better predict measured values. However, very small pores induce a negligible softening effect on samples. In these cases (e.g., sample 1.2, $\phi = 0.02\%$) the measured and predicted effective Young's modulus lie within the range of measurements of solid sample modulus, which makes this comparison meaningless. A pore volume fraction of above $\approx 1\%$ induces a measurable softening effect, and is therefore interesting for EMT evaluation purposes. We obtained errors of less than 5% with respect to predictions for samples with either $\phi = 1.4\%$ or $\phi = 2.8\%$ (samples 2.3, 2.5, 2.6, 2.8, 2.10, 2.11) and for $\phi = 5.2\%$, if the pore is spherical (sample 2.1).

Figure 16. Ranges of predictions for FDM samples based on background Young's modulus, $E_0 = 2.69$ GPa, and background Poisson's ratio, $\nu_0 = 0.41$. The range of prediction increase with the augmentation of the radius of the designed crack, and with the decrease of the aspect ratio of the ellipsoid.
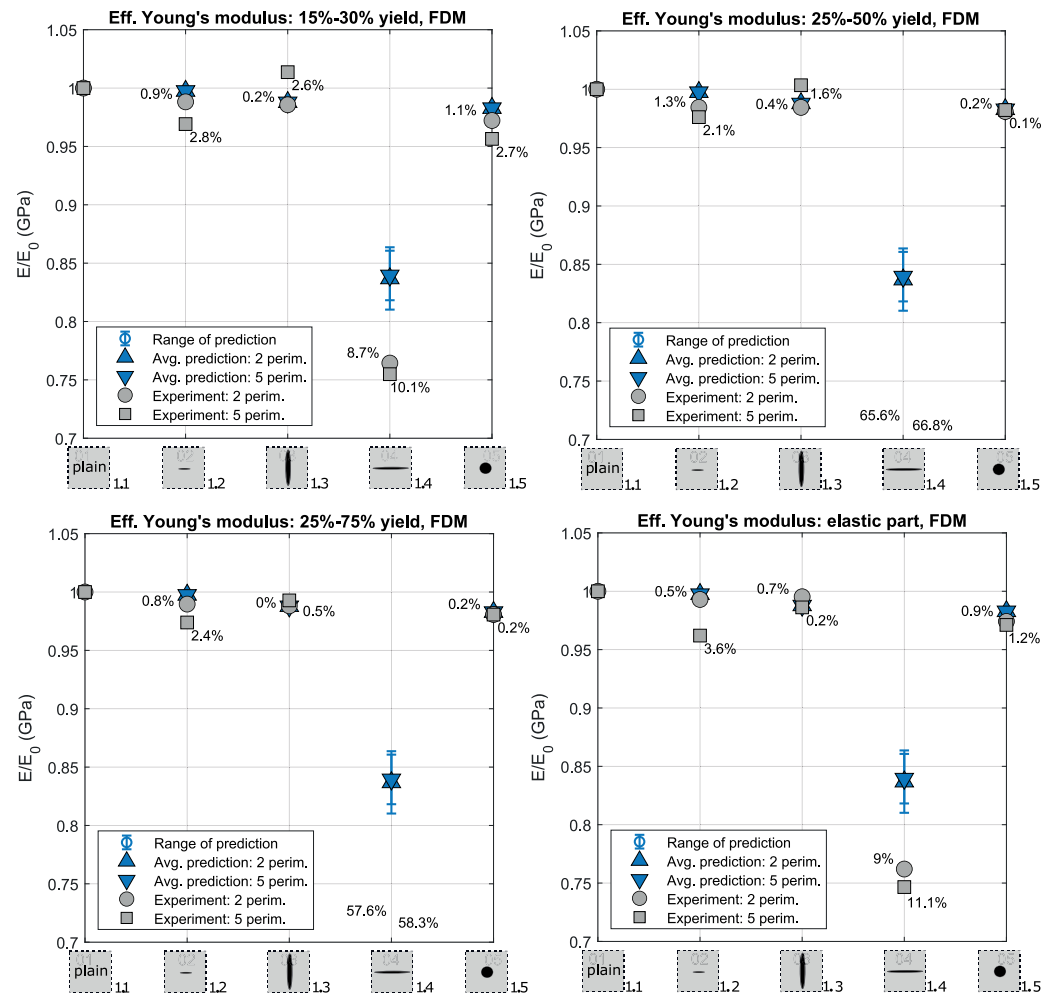
Figure 17. Effective Young's moduli obtained from compression tests of FDM samples (arithmetic mean of results from six tested prints per sample type). Results are normalized by Young's modulus of the average solid core taken from Table 6. Samples have either two or five perimeters. Each figure corresponds to different measures of Young's moduli. The relative error [%] between mean EMT predictions and mean uniaxial results are presented. The best fit, on average 2.73%, appears for Young's moduli measured within the 15%–30% yield range and for samples having two perimeters.

Interestingly, a good fit between measurements and predictions was also obtained for overlapping pores (e.g., samples 2.8, 2.10, 2.11), in which the NIA is non-valid. Overall, experimental results show that closer interactions augment measured effective elasticity as compared to samples where voids are not overlapping, resulting in EMT predictions underestimating the effective properties of samples with interacting pores. Such underestimation is expected if local shielding effect is present.

It is also relevant to note that although the volume of the oblate, horizontal pores in samples 1.4 and 2.4 are the same, the increased aspect ratio of the pore in sample 2.4 (0.2) with respect to sample 1.4 (0.1) reduced the distance between void boundary and sample edge by 1 mm, which was enough to avoid the edge effect and a deformation mechanism dominated by pore space collapse. A distance of ≈ 4 mm from pore boundary to the sample edge is therefore recommended to avert pore collapse.

Finally, the mean error between predicted and measured effective moduli considering samples 1–13 of the secondary printing phase lie between 2% and 5% (Table B3, column 16). This averaged error increases to up to 25% when also considering samples 2.14, 2.15 (Table B3, column 17). These results highlight the strengths of EMT for predicting the effective properties of solids containing large, and even interacting, voids, as long as the

Figure 18. Effective Young's moduli obtained from compression tests of SLA samples (arithmetic mean of results from three tested prints per sample type). Results are normalized by Young's modulus of the average solid core taken from Table B2. Samples were cured for a month (m), week (w), or were heated (h) with a short cure (up to 2 days). Each figure corresponds to different measures of Young's moduli. The relative differences [%] between mean EMT predictions and mean uniaxial results are presented. The best fit, on average 4.07%, appears for Young's moduli measured within the elastic range and for samples being cured for a month.

pore volume fraction lies below $\approx 5\%$. The prediction is even better if we do not consider samples with strong shielding effect. Namely, considering samples without stacked horizontal and oblate pores, 2.1–2.8, and 2.10–2.11, the mean relative error lies between 2% and 3%.

5.3. Future Perspectives: Pore-Fluid Injection Into 3D Printed Samples for Undrained Poroelasticity Tests

When porous, elastic materials saturated with fluids are subjected to stress changes that may reduce or increase the volume of pore space, the fluids within them experience a change in pore fluid pressure, which can significantly influence the strength and deformation of materials (Biot, 1941, 1955). The most significant poroelastic effects occur in "undrained" conditions, that is, when fluids are trapped within a poorly connected pore space and cannot immediately flow in response to stress changes. The undrained poroelastic response of a material subjected to a change in mean stress can be predicted using the relation (Rice & Cleary, 1976; Skempton, 1954):
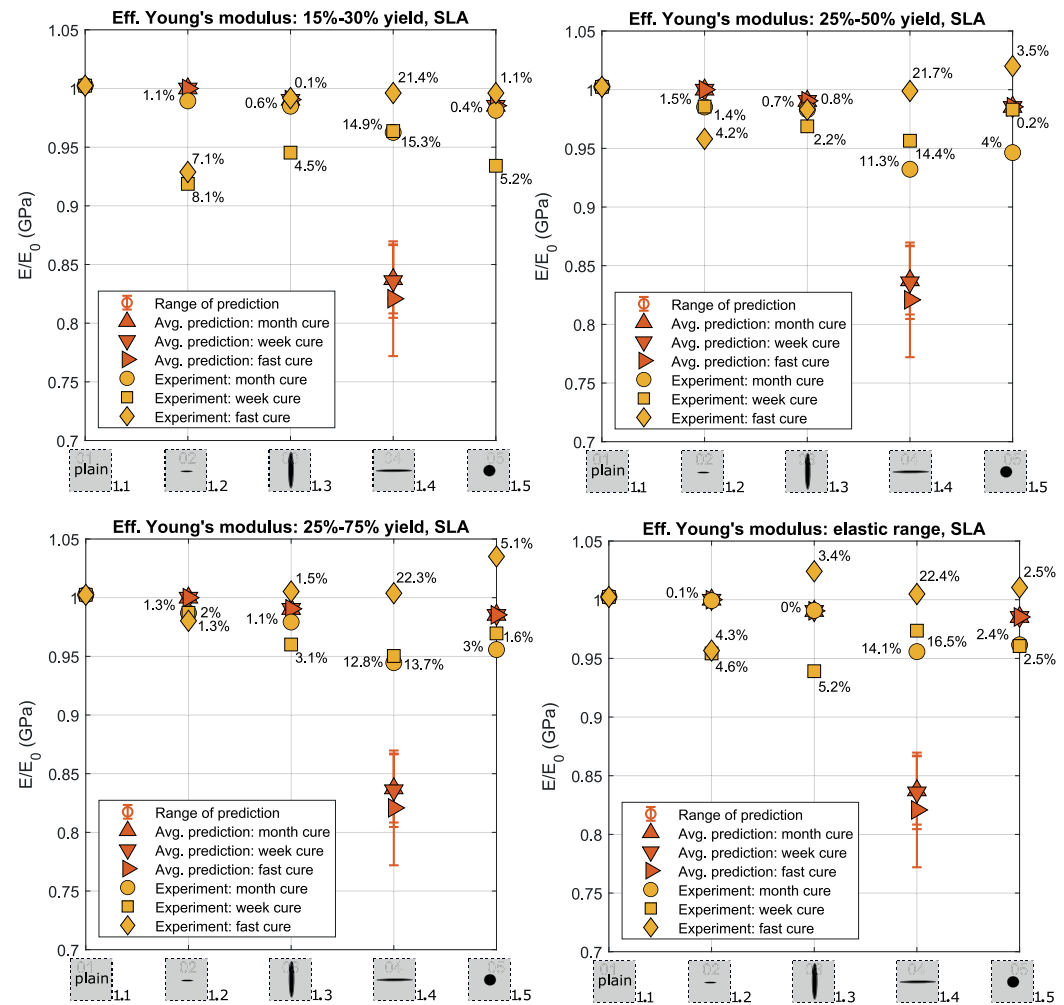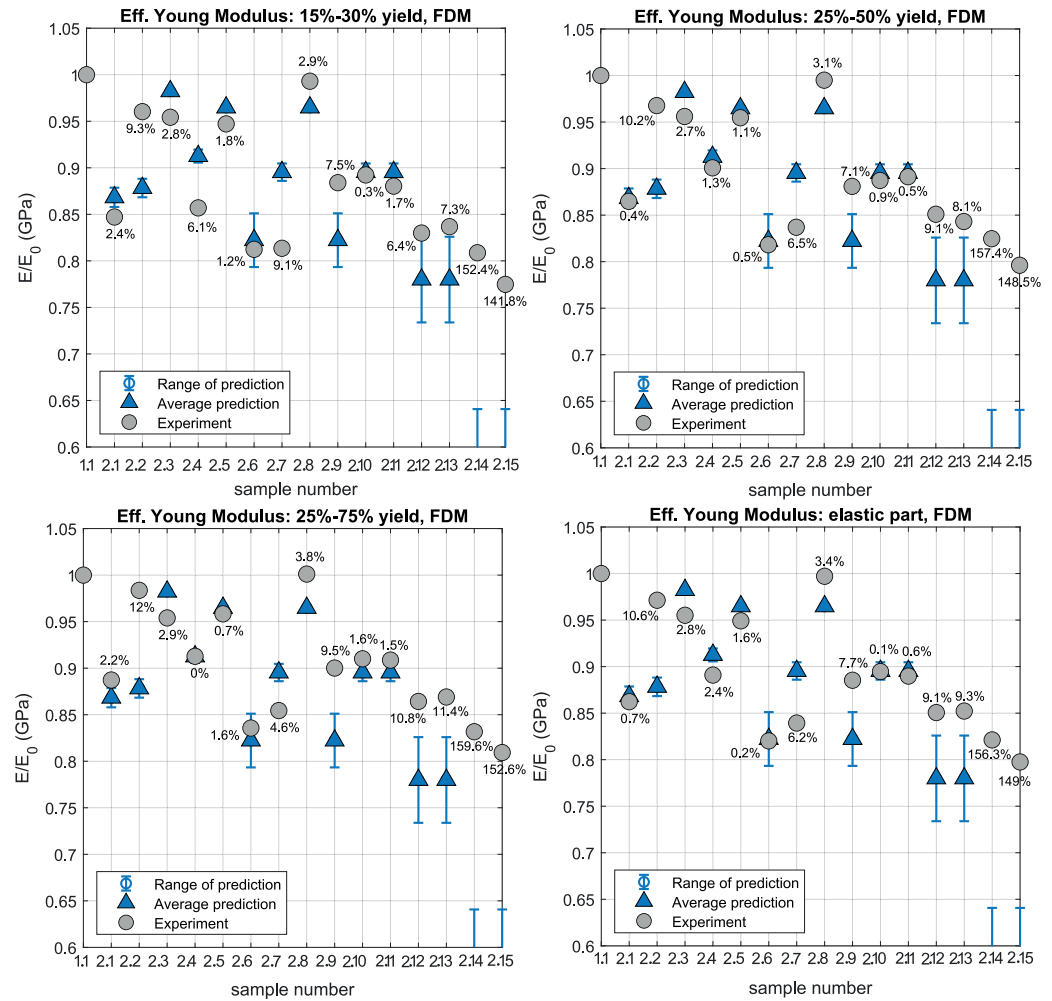
Figure 19. Effective Young's moduli obtained from compressions of FDM solid samples (arithmetic mean of results from 12 tested prints) and 15 types of FDM cores with designed voids (arithmetic mean of results from six tested prints per sample type). All samples have two perimeters. Each figure corresponds to different measures of Young's moduli. The relative error [%] between mean EMT predictions and mean uniaxial results are presented. The best fit, on average 23.6%, appears for Young's moduli measured within the 15%–30% yield range.

$$\Delta p_u = B\Delta \sigma_m \tag{9}$$

where Δp_u is the change in pore fluid pressure, $\Delta \sigma_m$ the change in mean stress, and B is the Skempton's coefficient, a scalar for isotropic materials and a tensor for anisotropic solids and/or with an anisotropic pore space (Wang, 2000). Obtaining direct measurements of B in the laboratory is a challenging feat, even for the "simple" isotropic case. As a result, the effect of pore space fabric on the poroelastic response of materials has been only predicted by means of theoretical simulations (Sayers & Kachanov, 1995).

3D printed samples with voids would enable the injection of pore fluids into their isolated pores and to conduct compression experiments while measuring in situ pore fluid pressure change, using methods adapted from Brantut and Aben (2021) and/or Proctor et al. (2020). This workflow would lead to direct quantification of poroelastic parameters, which added to the absolute control of pore space fabric that 3D printing methods offer, would allow to fully describe the effect of pore geometry anisotropy on the poroelastic response of materials. This overarching goal constitutes the major motivation for the present study, and is currently a work in progress.

6. Conclusions

We have fabricated over two hundred 3D printed samples with relatively large voids of different sizes and geometries, using two printing technologies and various specifications, and compared their measured effective properties with predictions from EMT. From this large amount of data, we can conclude that both FDM and SLA printing technologies can emulate homogeneous solids with voids whose effective elastic properties can be predicted by EMT with an error of less than 5%, if certain specifications and considerations are taken into account:

- Best results for FDM printed samples are obtained by specifying two contour printing perimeters, and when 15%–30% of the stress/strain curve is considered for effective elastic modulus computation.
- Best results for SLA printed samples are obtained by longer, post-printing, curing times (1 month in our case).
- Although the accuracy obtained for SLA and FDM samples can be similar, the lower cost of FDM, added to the necessity of long curing times plus identified issues with repeatability and recyclability for SLA printed samples, makes FDM overall more convenient for the manufacture of solids with voids.
- The pore volume fraction of the designed porous samples needs to be above 1% to induce a measurable softening effect. However, a pore volume fraction above 5% results in equivocal, wide range of estimation by EMT that fails to predict the measured effective moduli of samples.
- Better fits are obtained for spherical pores with respect to horizontally and vertically oriented pores.
- Close interactions between voids leads to a diminished softening effect that is thus overestimated by EMT predictions. This might be caused by local shielding excluded from effective approximations.
- A minimum distance of 16% of the sample diameter from the pore boundary to the sample edge should be prescribed for FDM printed samples to avoid an inelastic deformation mechanism through pore space collapse.

Appendix A: Contribution Tensors for Spheroidal Void

Compliance contribution tensor, $H_{ijk\ell}$, responsible for an increase of compliance due to void presence can be written as

$$H_{ijk\ell} = \left(C^0_{ijmn} - C^0_{ijmn} P_{mnrs} C^0_{rsk\ell} \right)^{-1}, \tag{A1}$$

where C^0_{ijmn} is the background stiffness tensor and P_{mnrs} is Hill's tensor. The stiffness contribution tensor, $N_{ijk\ell}$, responsible for a decrease of stiffness due to void presence can be written as

$$N_{ijk\ell} = \left(P_{ijk\ell} - S^0_{ijk\ell} \right)^{-1}, \tag{A2}$$

where $S^0_{ijK\ell}$ is the background compliance tensor (Kachanov & Sevostianov, 2018).

If a void is a spheroid ($a = a_2 = a_3$), the components of Hill's tensor can be written as

$$P_{1111} = \frac{2(1+\nu)}{E}\left[(1-\kappa)(1-2f_0) + 2\kappa f_1\right], \qquad P_{2222} = P_{3333} = \frac{1+\nu}{2E}\left[(4-3\kappa)f_0 + 3\kappa f_1\right], \tag{A3}$$

$$P_{2233} = P_{3322} = \frac{\kappa(1+\nu)}{2E}(f_1 - f_0), \qquad P_{1122} = P_{2211} = P_{1133} = P_{3311} = \frac{-2\kappa(1+\nu)}{E}f_1, \tag{A4}$$

$$P_{2323} = \frac{1+\nu}{2E}\left[(2-\kappa)f_0 + \kappa f_1\right], \qquad P_{1212} = P_{1313} = \frac{1+\nu}{2E}(1 - f_0 - 4\kappa f_1), \tag{A5}$$

where E is Young's modulus, ν is Poisson's ratio, $\kappa = 1/[2(1-\nu)]$, and

$$f_0 = \frac{1-g}{2(1-\gamma^2)}, \qquad f_1 = \frac{(2+\gamma^2)g - 3\gamma^2}{4(1-\gamma^2)^2}, \tag{A6}$$

where γ is aspect ratio and

$$g = \begin{cases} \dfrac{1}{\gamma\sqrt{1-\gamma^2}}\arctan\dfrac{\sqrt{1-\gamma^2}}{\gamma}, & \text{for oblate shape } (\gamma \geq 1) \\ \dfrac{1}{\gamma\sqrt{\gamma^2-1}}\ln\left(\gamma+\sqrt{\gamma^2-1}\right), & \text{for prolate shape } (\gamma \leq 1) \end{cases}. \tag{A7}$$

Hill's tensor is transversely isotropic, its components are consistent with Kachanov and Sevostianov (2018) derivations, however, in our case the x_1-axis, (not the x_3-axis) is the rotational symmetry axis.

Appendix B: Tables

Table B1

Mean Experimental (exp.) and Theoretical (th.) Young's Moduli for Five FDM Sample Types, Along With the Span of the Experimental Results, Range of Theoretical Predictions, and the Relative Errors

	1.1_t	1.2_t	1.3_t	1.4_t	1.5_t	$1.1_t{-}1.5_t$	1.1_v	1.2_v	1.3_v	1.4_v	1.5_v	$1.1_v{-}1.5_v$
exp. E_{15-30}	2.69	2.66	2.65	2.06	2.62	2.54	2.64	2.56	2.68	1.99	2.53	2.48
exp. span	0.31	0.26	0.29	0.23	0.18	–	0.33	0.35	0.30	0.14	0.14	–
th. E_{15-30}	–	2.69	2.66	2.25	2.65	2.60	–	2.63	2.61	2.22	2.60	2.51
th. range	–	±0.00	±0.00	±0.07	±0.00	–	–	±0.00	±0.00	±0.06	±0.00	–
$\lvert R\rvert^{m}_{15-30}$ [%]	–	0.94	0.23	8.66	1.08	2.73	–	2.84	2.62	10.1	2.68	4.55
$\lvert R\rvert^{cls}_{15-30}$ [%]	–	0.94	0.22	5.65	1.07	1.97	–	2.84	2.62	7.74	2.66	3.97
exp. E_{25-50}	2.73	2.69	2.69	0.79	2.68	2.31	2.68	2.62	2.69	0.75	2.64	2.28
exp. span	0.19	0.19	0.21	0.11	0.16	–	0.31	0.32	0.16	0.11	0.15	–
th. E_{25-50}	–	2.72	2.69	2.28	2.68	2.60	–	2.68	2.65	2.25	2.64	2.55
th. range	–	±0.00	±0.00	±0.07	±0.00	–	–	±0.00	±0.00	±0.06	±0.00	–
$\lvert R\rvert^{m}_{25-50}$ [%]	–	1.31	0.35	65.6	0.20	16.9	–	2.14	1.59	66.8	0.06	17.6
$\lvert R\rvert^{cls}_{25-50}$ [%]	–	1.31	0.34	64.4	0.19	16.6	–	2.14	1.58	65.9	0.04	17.4
exp. E_{25-75}	2.64	2.61	2.61	0.94	2.59	2.27	2.61	2.54	2.59	0.91	2.56	2.24
exp. span	0.23	0.10	0.18	0.07	0.10	–	0.32	0.23	0.20	0.10	0.11	–
th. E_{25-75}	–	2.63	2.60	2.21	2.59	2.51	–	2.60	2.58	2.19	2.56	2.48
th. range	–	±0.00	±0.00	±0.07	±0.00	–	–	±0.00	±0.00	±0.06	±0.00	–
$\lvert R\rvert^{m}_{25-75}$ [%]	–	0.79	0.02	57.6	0.22	14.7	–	2.36	0.52	58.3	0.21	15.4
$\lvert R\rvert^{cls}_{25-75}$ [%]	–	0.79	0.01	56.2	0.20	14.3	–	2.36	0.51	57.2	0.20	15.1
exp. E_{el}	2.63	2.61	2.61	2.00	2.56	2.48	2.59	2.49	2.56	1.94	2.52	2.42
exp. span	0.17	0.17	0.24	0.33	0.15	–	0.29	0.28	0.19	0.25	0.24	–
th. E_{el}	–	2.62	2.60	2.20	2.58	2.50	–	2.59	2.56	2.18	2.55	2.47
th. range	–	±0.00	±0.00	±0.07	±0.00	–	–	±0.00	±0.00	±0.06	±0.00	–
$\lvert R\rvert^{m}_{el}$ [%]	–	0.46	0.75	8.95	0.88	2.76	–	3.55	0.15	11.1	1.18	3.99
$\lvert R\rvert^{cls}_{el}$ [%]	–	0.46	0.74	5.95	0.86	2.00	–	3.55	0.14	8.76	1.17	3.40

Note. Samples have either two (subscript t) or five perimeters (subscript v). Predictions are made based on mean Young's moduli and Poisson's ratios of solid samples (1.1_t or 1.1_v). $\lvert R\rvert^{m}_{Y}$ stands for the relative error of the mean prediction (central value within the predicted Young's modulus range) with respect to the mean measurement, $\lvert R\rvert^{cls}_{Y}$ denotes the relative error of the closest prediction (value within the predicted Young's modulus range) with respect to the mean measurement, where Y is replaced by $15{-}30$, $25{-}50$, $25{-}75$, or "el" indicating Young's moduli calculation method.

Table B2
Mean Experimental (exp.) and Theoretical (th.) Young's Moduli for Five SLA Sample Types, Along With the Span of the Experimental Results, Range of Theoretical Predictions, and the Relative Errors

	1.1_m	1.2_m	1.3_m	1.4_m	1.5_m	$1.1_m-1.5_m$	1.1_w	1.2_w	1.3_w	1.4_w	1.5_w	$1.1_w-1.5_w$	1.1_f	1.2_f	1.3_f	1.4_f	1.5_f	$1.1_f-1.5_f$
exp. E_{15-30}	1.45	1.43	1.42	1.39	1.42	1.42	1.20	1.10	1.14	1.16	1.12	1.15	1.52	1.41	1.51	1.51	1.51	1.49
exp. span	0.07	0.06	0.10	0.04	0.15	–	0.12	0.29	0.06	0.09	0.08	–	0.11	0.06	0.12	0.11	0.03	–
th. E_{15-30}	–	1.44	1.43	1.21	1.42	1.38	–	1.20	1.19	1.00	1.18	1.15	–	1.52	1.51	1.25	1.50	1.44
th. range	–	±0.00	±0.00	±0.04	±0.00	–	–	±0.00	±0.00	±0.04	±0.00	–	–	±0.00	±0.00	±0.07	±0.00	–
$|R|^m_{15-30}$ [%]	–	1.06	0.55	14.9	0.39	4.24	–	8.13	4.54	15.3	5.19	8.29	–	7.11	0.13	21.4	1.09	7.42
$|R|^{cls}_{15-30}$ [%]	–	1.06	0.55	11.1	0.37	3.27	–	8.13	4.53	11.1	5.17	7.24	–	7.11	0.12	14.5	1.07	5.71
exp. E_{25-50}	1.44	1.42	1.41	1.34	1.36	1.39	1.14	1.12	1.10	1.09	1.12	1.12	1.47	1.40	1.44	1.46	1.49	1.45
exp. span	0.09	0.06	0.09	0.09	0.12	–	0.07	0.14	0.02	0.01	0.02	–	0.13	0.10	0.05	0.11	0.05	–
th. E_{25-50}	–	1.44	1.42	1.20	1.42	1.37	–	1.14	1.13	0.95	1.12	1.09	–	1.47	1.45	1.20	1.44	1.39
th. range	–	±0.00	±0.00	±0.04	±0.00	–	–	±0.00	±0.00	±0.04	±0.00	–	–	±0.00	±0.00	±0.07	±0.00	–
$|R|^m_{25-50}$ [%]	–	1.47	0.74	11.3	3.95	4.37	–	1.44	2.19	14.4	0.23	4.57	–	4.20	0.76	21.7	3.51	7.54
$|R|^{cls}_{25-50}$ [%]	–	1.47	0.73	7.57	3.94	3.43	–	1.44	2.18	10.3	0.21	3.53	–	4.20	0.75	14.8	3.49	5.82
exp. E_{25-75}	1.30	1.28	1.27	1.22	1.24	1.26	1.03	1.02	0.99	0.98	1.00	1.00	1.29	1.26	1.30	1.30	1.34	1.30
exp. span	0.08	0.05	0.08	0.08	0.11	–	0.08	0.11	0.05	0.03	0.04	–	0.12	0.10	0.11	0.10	0.03	–
th. E_{25-75}	–	1.29	1.28	1.08	1.28	1.23	–	1.03	1.02	0.86	1.01	0.98	–	1.29	1.28	1.06	1.27	1.22
th. range	–	±0.00	±0.00	±0.04	±0.00	–	–	±0.00	±0.00	±0.03	±0.00	–	–	±0.00	±0.00	±0.06	±0.00	–
$|R|^m_{25-75}$ [%]	–	1.31	1.12	12.8	3.00	4.56	–	1.29	3.07	13.7	1.60	4.91	–	1.97	1.48	22.3	5.05	7.70
$|R|^{cls}_{25-75}$ [%]	–	1.31	1.11	9.01	2.99	3.60	–	1.28	3.06	9.59	1.58	3.88	–	1.97	1.48	15.4	5.03	5.97
exp. E_{el}	1.39	1.38	1.37	1.32	1.33	1.36	1.13	1.08	1.06	1.10	1.09	1.09	1.46	1.39	1.49	1.46	1.47	1.45
exp. span	0.05	0.06	0.05	0.08	0.12	–	0.09	0.19	0.06	0.02	0.02	–	0.14	0.11	0.12	0.12	0.09	–
th. E_{el}	–	1.39	1.37	1.16	1.36	1.32	–	1.13	1.12	0.94	1.11	1.08	–	1.46	1.44	1.19	1.43	1.38
th. range	–	±0.00	±0.00	±0.04	±0.00	–	–	±0.00	±0.00	±0.04	±0.00	–	–	±0.00	±0.00	±0.07	±0.00	–
$|R|^m_{el}$ [%]	–	0.08	0.05	14.1	2.40	4.16	–	4.58	5.18	16.5	2.52	7.19	–	4.33	3.40	22.4	2.55	8.18
$|R|^{cls}_{el}$ [%]	–	0.08	0.04	10.3	2.38	3.20	–	4.58	5.16	12.3	2.50	6.13	–	4.33	3.40	15.5	2.53	6.45

Note. Samples are cured for a month (subscript m), a week (subscript w), or are fast-cured and heated (subscript f). Predictions are made based on mean Young's moduli and Poisson's ratios of solid samples (1.1_m, 1.1_w, or 1.1_f). $|R|^m_Y$ stands for the relative error of the mean prediction (central value within the predicted Young's modulus range) with respect to the mean measurement, $|R|^{cls}_Y$ denotes the relative error of the closest prediction (value within the predicted Young's modulus range) with respect to the mean measurement, where Y is replaced by 15–30, 25–50, 25–75, or "el" indicating Young's moduli calculation method.

Table B3
Mean Experimental (exp.) and Theoretical (th.) Young's Moduli for Fifteen FDM Sample Types, Along With the Span of the Experimental Results, Range of Theoretical Predictions, and the Relative Errors

	2.1	2.2	2.3	2.4	2.5	2.6	2.7	2.8	2.9	2.10	2.11	2.12	2.13	2.14	2.15	2.1–2.13	2.1–2.15
exp. E_{15-30}	2.28	2.58	2.57	2.31	2.55	2.19	2.19	2.67	2.38	2.40	2.37	2.23	2.25	2.18	2.09	2.38	2.35
exp. span	0.15	0.15	0.62	0.40	0.58	0.34	0.79	0.34	0.17	0.27	0.26	0.35	0.09	0.16	0.12	–	–
th. E_{15-30}	2.34	2.36	2.64	2.46	2.60	2.21	2.41	2.60	2.21	2.41	2.41	2.10	2.10	0.86	0.86	2.37	2.17
th. range	±0.03	±0.03	±0.00	±0.02	±0.00	±0.08	±0.03	±0.00	±0.08	±0.03	±0.03	±0.12	±0.12	±0.86	±0.86	–	–
$|R|^m_{15-30}$ [%]	2.43	9.34	2.84	6.10	1.83	1.20	9.13	2.93	7.51	0.34	1.68	6.41	7.29	152	142	4.54	23.6
$|R|^{cls}_{15-30}$ [%]	1.26	8.12	2.83	5.37	1.76	0	8.18	2.86	3.86	0	0.64	0.48	1.31	26.2	20.9	2.82	5.58
exp. E_{25-50}	2.36	2.64	2.61	2.46	2.60	2.23	2.28	2.71	2.40	2.42	2.43	2.32	2.30	2.25	2.17	2.44	2.41
exp. span	0.21	0.20	0.64	0.37	0.42	0.22	0.82	0.22	0.12	0.19	0.26	0.26	0.19	0.17	0.19	–	–
th. E_{25-50}	2.37	2.40	2.68	2.49	2.63	2.24	2.44	2.63	2.24	2.44	2.44	2.13	2.13	0.87	0.87	2.40	2.20
th. range	±0.03	±0.03	±0.00	±0.02	±0.00	±0.08	±0.03	±0.00	±0.08	±0.03	±0.03	±0.13	±0.13	±0.87	±0.87	–	–
$|R|^m_{25-50}$ [%]	0.40	10.2	2.67	1.29	1.05	0.50	6.52	3.14	7.14	0.90	0.45	9.12	8.11	157	149	3.96	23.8
$|R|^{cls}_{25-50}$ [%]	0	8.95	2.65	0.53	0.99	0	5.53	3.07	3.51	0	0	3.04	2.08	28.7	24.3	2.33	5.56
exp. E_{25-75}	2.34	2.59	2.52	2.41	2.53	2.20	2.25	2.64	2.37	2.40	2.40	2.28	2.29	2.19	2.13	2.40	2.37
exp. span	0.20	0.21	0.66	0.32	0.39	0.22	0.77	0.26	0.14	0.19	0.27	0.27	0.19	0.14	0.17	–	–
th. E_{25-75}	2.29	2.32	2.59	2.41	2.54	2.17	2.36	2.54	2.17	2.36	2.36	2.06	2.06	0.84	0.84	2.32	2.13
th. range	±0.03	±0.03	±0.00	±0.02	±0.00	±0.08	±0.02	±0.00	±0.08	±0.02	±0.02	±0.12	±0.12	±0.84	±0.84	–	–
$|R|^m_{25-75}$ [%]	2.18	12.0	2.87	0.02	0.67	1.63	4.57	3.77	9.47	1.65	1.49	10.8	11.4	160	153	4.81	25.0
$|R|^{cls}_{25-75}$ [%]	0.98	10.8	2.86	0	0.60	0	3.56	3.70	5.76	0.60	0.44	4.64	5.22	29.8	26.3	3.01	6.35
exp. E_{el}	2.27	2.55	2.51	2.34	2.49	2.15	2.21	2.62	2.33	2.35	2.34	2.23	2.24	2.16	2.10	2.36	2.33
exp. span	0.24	0.14	0.71	0.38	0.54	0.36	0.83	0.23	0.09	0.19	0.27	0.23	0.13	0.18	0.22	–	–
th. E_{el}	2.28	2.31	2.58	2.40	2.53	2.16	2.35	2.53	2.16	2.35	2.35	2.05	2.05	0.84	0.84	2.32	2.12
th. range	±0.03	±0.03	±0.00	±0.02	±0.00	±0.08	±0.02	±0.00	±0.08	±0.02	±0.02	±0.12	±0.12	±0.84	±0.84	–	–
$|R|^m_{el}$ [%]	0.69	10.6	2.75	2.37	1.61	0.25	6.25	3.35	7.68	0.07	0.61	9.07	9.28	156	149	4.20	24.0
$|R|^{cls}_{el}$ [%]	0	9.36	2.74	1.62	1.55	0	5.26	3.28	4.03	0	0	2.99	3.19	28.2	24.5	2.62	5.78

Note. Predictions are made based on mean Young's moduli and Poisson's ratios of a solid sample 1.1$_r$. $|R|^m_{|Y}$ stands for the relative error of the mean prediction (central value within the predicted Young's modulus range) with respect to the mean measurement, $|R|^{cls}_{|Y}$ denotes the relative error of the closest prediction (value within the predicted Young's modulus range) with respect to mean measurement, where Y is replaced by 15–30, 25–50, 25–75, or "el" indicating Young's moduli calculation method.

Conflict of Interest

The authors declare no conflicts of interest relevant to this study.

Data Availability Statement

All raw data files obtained in this study can be downloaded from Stanton-Yonge (2024).

References

Backus, G. E. (1962). Long-wave elastic anisotropy produced by horizontal layering. *Journal of Geophysical Research*, *67*(11), 4427–4440. https://doi.org/10.1029/jz067i011p04427

Biot, M. A. (1941). General theory of three-dimensional consolidation. *Journal of Applied Physics*, *12*(2), 155–164. https://doi.org/10.1063/1.1712886

Biot, M. A. (1955). Theory of elasticity and consolidation for a porous anisotropic solid. *Journal of Applied Physics*, *26*(2), 182–185. https://doi.org/10.1063/1.1721956

Brantut, N., & Aben, F. M. (2021). Fluid pressure heterogeneity during fluid flow in rocks: New laboratory measurement device and method. *Geophysical Journal International*, *225*(2), 968–983. https://doi.org/10.1093/gji/ggab019

Brantut, N., & Petit, L. (2022). Micromechanics of rock damage and its recovery in cyclic loading conditions. *Geophysical Journal International*, *233*(1), 145–161. https://doi.org/10.1093/gji/ggac447

Bristow, J. R. (1960). Microcracks, and the static and dynamic elastic constants of annealed and heavily cold-worked metals. *Journal of Applied Physics*, *11*(2), 81–85. https://doi.org/10.1088/0508-3443/11/2/309

Bruggeman, D. A. G. (1937). Berechnung verschiedener physikalischer Konstanten von heterogenen Substanzen. III. Die elastischen Konstanten der quasiisotropen Mischkör-per aus isotropen Substanzen. *Annalen der Physik*, *421*(2), 160–178. https://doi.org/10.1002/andp.19374210205

Budiansky, B. (1965). On the elastic moduli of some heterogeneous materials. *Journal of the Mechanics and Physics of Solids*, *13*(4), 223–227. https://doi.org/10.1016/0022-5096(65)90011-6

Chockalingam, K., Jawahar, N., & Chandrasekhar, U. (2006). Influence of layer thickness on mechanical properties in stereolithography. *Rapid Prototyping Journal*, *12*(2), 106–113. https://doi.org/10.1108/13552540610652456

Cosenza, P., Fauchille, A.-L., Prêt, D., Hedan, S., & Giraud, A. (2019). Statistical representative elementary area of shale inferred by micromechanics. *International Journal of Engineering Science*, *142*, 53–73. https://doi.org/10.1016/j.ijengsci.2019.05.012

Dean, G., Loveday, M., Cooper, P., Read, B., Roebuck, B., & Morrell, R. (1995). Aspects of modulus measurement. In *Materials metrology and standards for structural performance* (pp. 150–209).

Dizon, J. R. C., Espera, A. H., Chen, Q., & Advincula, R. C. (2018). Mechanical characterization of 3d-printed polymers. *Additive Manufacturing*, *20*, 44–67. https://doi.org/10.1016/j.addma.2017.12.002

Dugarov, G. A., Kolesnikov, Y. I., Fedin, K. V., Orlov, Y. A., & Ngomayezwe, L. (2022). Acoustic measurements on synthetic fractured samples made using FDM 3D printing technology. *Processes in GeoMedia*, *4*, 9–16.

Eshelby, J. D. (1957). The determination of the elastic field of an ellipsoidal inclusion, and related problems. *Proceedings of the Royal Society A: Mathematical, Physical and Engineering Sciences*, *241*, 376–396.

Hashin, Z. (1959). The moduli of an elastic solid, containing spherical particles of another elastic material. *Nonhomogeneity in Elasticity and Plasticity*, *9*, 463–478.

Henriques, J. P., de Figueiredo, J. J. S., Santos, L. K., Macedo, D. L., Coutinho, I., da Silva, C. B., et al. (2018). Experimental verification of effective anisotropic crack theories in variable crack aspect ratio medium. *Geophysical Prospecting*, *66*(1), 141–156. https://doi.org/10.1111/1365-2478.12544

Hill, R. (1952). The elastic behaviour of a crystalline aggregate. *Proceedings of the Physical Society Section A*, *65*(5), 349–354. https://doi.org/10.1088/0370-1298/65/5/307

Hill, R. (1965). A self-consistent mechanics of composite materials. *Journal of the Mechanics and Physics of Solids*, *13*(4), 213–222. https://doi.org/10.1016/0022-5096(65)90010-4

Huang, L., Stewart, R. R., Dyaur, N., & Baez-Franceschi, J. (2016). 3D-printed rock models: Elastic properties and the effects of penny-shaped inclusions with fluid substitution. *Geophysics*, *81*(6), 1ND–Z53. https://doi.org/10.1190/geo2015-0655.1

Huet, C. (1990). Application of variational concepts to size effects in elastic heterogeneous bodies. *Journal of the Mechanics and Physics of Solids*, *38*(6), 813–841. https://doi.org/10.1016/0022-5096(90)90041-2

Kachanov, M. (1980). Continuum model of medium with cracks. *Journal of Engineering Mechanics*, *106*(5), 1039–1051. https://doi.org/10.1061/jmcea3.0002642

Kachanov, M. (1992). Effective elastic properties of cracked solids: Critical review of some basic concepts. *Applied Mechanics Reviews*, *45*(8), 304–335. https://doi.org/10.1115/1.3119761

Kachanov, M., & Sevostianov, I. (2018). *Micromechanics of materials, with applications*. Springer.

Kazmer, D. (2017). Three-dimensional printing of plastics. In *Applied plastics engineering handbook* (pp. 617–634). Elsevier.

Li, Y., Linke, B. S., Voet, H., Falk, B., Schmitt, R., & Lam, M. (2017). Cost, sustainability and surface roughness quality–a comprehensive analysis of products made with personal 3d printers. *CIRP Journal of Manufacturing Science and Technology*, *16*, 1–11. https://doi.org/10.1016/j.cirpj.2016.10.001

Li, Z., & Lambros, J. (2001). Strain rate effects on the thermomechanical behavior of polymers. *International Journal of Solids and Structures*, *38*(20), 3549–3562. https://doi.org/10.1016/s0020-7683(00)00223-7

Malkowski, P., Ostrowski, L., & Brodny, J. (2018). Analysis of Young's modulus for Carboniferous sedimentary rocks and its relationship with uniaxial compressive strength using different methods of modulus determination. *Journal of Sustainable Mining*, *17*(3), 145–157. https://doi.org/10.1016/j.jsm.2018.07.002

Mallet, C., Fortin, J., Guéguen, Y., & Bouyer, F. (2013). Effective elastic properties of cracked solids: An experimental investigation. *International Journal of Fracture*, *182*(2), 275–282. https://doi.org/10.1007/s10704-013-9855-y

Markov, M., Kazatchenko, E., & Mousatov, A. (2006). Compressional and shear wave velocities in multicomponent carbonate media as porosity functions. In *SPWLA Annual Logging Symposium*. SPWLA–2006.

Mohamed, O. A., Masood, S. H., & Bhowmik, J. L. (2015). Optimization of fused deposition modeling process parameters: A review of current research and future prospects. *Advances in Manufacturing*, *3*(1), 42–53. https://doi.org/10.1007/s40436-014-0097-7

Ndao, B., Do, D.-P., & Hoxha, D. (2017). P- and S-wave anisotropy to characterise and quantify damage in media: Laboratory experiment using synthetic sample with aligned microcracks. *Geophysical Prospecting*, *65*(S1), 181–200. https://doi.org/10.1111/1365-2478.12546

O'Connell, R. J., & Budiansky, B. (1974). Seismic velocities in dry and saturated cracked solids. *Journal of Geophysical Research*, *79*(35), 5412–5426. https://doi.org/10.1029/jb079i035p05412

Oda, M., Suzuki, K., & Maeshibu, T. (1984). Elastic compliance for rock-like materials with random cracks. *Soils and Foundations*, *24*(3), 27–40. https://doi.org/10.3208/sandf1972.24.3_27

Paterson, M., & Wong, T.-F. (2005). *Experimental rock deformation—The brittle field* (2nd ed.). Springer.

Peloquin, J., Han, Y., & Gall, K. (2023). Printability and mechanical behavior as a function of base material, structure, and a wide range of porosities for polymer lattice structures fabricated by vat-based 3d printing. *Additive Manufacturing*, *78*, 103892. https://doi.org/10.1016/j.addma.2023.103892

Postma, G. W. (1955). Wave propagation in a stratified medium. *Geophysics*, *20*(4), 780–806. https://doi.org/10.1190/1.1438187

Proctor, B., Lockner, D., Kilgore, B., Mitchell, T., & Beeler, N. (2020). Direct evidence for fluid pressure, dilatancy, and compaction affecting slip in isolated faults. *Geophysical Research Letters*, *47*(16), e2019GL086767. https://doi.org/10.1029/2019gl086767

Reuss, A. (1929). Berechnung der Fließgrenze von Mischkristallen auf Grund der Plastizitätsbedingung für Einkristalle. *Zeitschrift für Angewandte Mathematik und Mechanik*, *9*(1), 49–58. https://doi.org/10.1002/zamm.19290090104

Rice, J. R., & Cleary, M. P. (1976). Some basic stress diffusion solutions for fluid-saturated elastic porous media with compressible constituents. *Reviews of Geophysics*, *14*(2), 227–241. https://doi.org/10.1029/rg014i002p00227

Santos, L. K., de Figueiredo, J. J. S., Macedo, D. L., de Melo, A. L., & da Silva, C. B. (2017). A new way to construct synthetic porous fractured medium. *Journal of Petroleum Science & Engineering*, *156*, 763–768. https://doi.org/10.1016/j.petrol.2017.06.044

Sayers, C., & Kachanov, M. (1991). A simple technique for finding effective elastic constants of cracked solids for arbitrary crack orientation statistics. *International Journal of Solids and Structures*, *7*(6), 671–680. https://doi.org/10.1016/0020-7683(91)90027-d

Sayers, C., & Kachanov, M. (1995). Microcrack-induced elastic wave anisotropy of brittle rocks. *Journal of Geophysical Research*, *100*(B3), 4149–4156. https://doi.org/10.1029/94jb03134

Schoenberg, M., & Douma, J. (1988). Elastic wave propagation in media with parallel fractures and aligned cracks. *Geophysical Prospecting*, *36*(6), 571–590. https://doi.org/10.1111/j.1365-2478.1988.tb02181.x

Schoenberg, M., & Helbig, K. (1997). Orthorhombic media: Modeling elastic wave behavior in a vertically fractured Earth. *Geophysics*, *62*(6), 1954–1974. https://doi.org/10.1190/1.1444297

Sevostianov, I., & Kachanov, M. (2010). Local minima and gradients of stiffness and conductivity as indicators of strength reduction of brittle-elastic materials. *International Journal of Fracture*, *164*(1), 147–154. https://doi.org/10.1007/s10704-010-9485-6

Shafiro, B., & Kachanov, M. (1997). Materials with fluid-filled pores of various shapes: Effective elastic properties and fluid pressure polarization. *International Journal of Solids and Structures*, *34*(27), 3517–3540. https://doi.org/10.1016/s0020-7683(96)00185-0

Skempton, A. (1954). The pore-pressure coefficients a and b. *Géotechnique*, *4*(4), 143–147. https://doi.org/10.1680/geot.1954.4.4.143

Stanton-Yonge, A. (2024). Data repository for uniaxial compression of 3d printed samples with voids: Laboratory measurements compared with effective medium theory. *Zenodo*. https://doi.org/10.5281/zenodo.13899448

Stewart, R. R., Dyaur, N., Omoboya, B., de Figueiredo, J. J. S., Willis, M., & Sil, S. (2013). Physical modeling of anisotropic domains: Ultrasonic imaging of laser-etched fractures in glass. *Geophysics*, *78*(1), 1JF–Z24. https://doi.org/10.1190/geo2012-0075.1

Voigt, W. (1889). Ueber die Beziehung zwischen den beiden Elastizitätskonstanten Isotroper Körper. *Annalen der Physik*, *274*(12), 573–587. https://doi.org/10.1002/andp.18892741206

Walsh, J. B. (1965). The effect of cracks on the compressibility of rock. *Journal of Geophysical Research*, *70*(2), 381–389. https://doi.org/10.1029/jz070i002p00381

Wang, H. (2000). *Theory of linear poroelasticity with applications to geomechanics and hydrogeology* (Vol. 2). Princeton university press. https://doi.org/10.1515/9781400885688

Zerhouni, O. (2019). *A study on the effective elastic properties of random porous materials: 3D printing, experiments and numerics* PhD Thesis. Institut Polytechnique de Paris.

Zerhouni, O., Tarantino, M., & Danas, K. (2019). Numerically-aided 3d printed random isotropic porous materials approaching the hashin-shtrikman bounds. *Composites Part B: Engineering*, *156*, 344–354. https://doi.org/10.1016/j.compositesb.2018.08.032

Zimmerman, R. W. (1986). The effect of cracks on the compressibility of rock. *Journal of Applied Mechanics*, *53*(3), 500–504. https://doi.org/10.1115/1.3171802